

Towards adaptive kinetic-fluid simulations of weakly ionized plasmas

V.I. Kolobov*, R.R. Arslanbekov

CFD Research Corporation, 215 Wynn Dr, Huntsville, AL 35805, USA

ARTICLE INFO

Article history:

Available online 23 July 2011

Keywords:

Boltzmann kinetic equation

Octree Cartesian mesh

Adaptive Mesh and Algorithm Refinement

Unified Flow Solver

Eulerian Vlasov solvers

Runaway electrons

Weakly ionized plasma

ABSTRACT

This paper describes an Adaptive Mesh and Algorithm Refinement (AMAR) methodology for multi-scale simulations of gas flows and the challenges associated with extending this methodology for simulations of weakly ionized plasmas. The AMAR method combines Adaptive Mesh Refinement (AMR) with automatic selection of kinetic or continuum solvers in different parts of computational domains. We first review the discrete velocity method for solving Boltzmann and Wang Chang–Uhlenbeck kinetic equations for rarefied gases. Then, peculiarities of AMR implementation with octree Cartesian mesh are discussed. A Unified Flow Solver (UFS) uses AMAR method with adaptive Cartesian mesh to dynamically introduce kinetic patches for multi-scale simulations of gas flows. We describe fluid plasma models with AMR capabilities and illustrate how physical models affect simulation results for gas discharges, especially in the areas where electron kinetics plays an important role. We introduce Eulerian solvers for plasma kinetic equations and illustrate the concept of adaptive mesh in velocity space. Specifics of electron kinetics in collisional plasmas are described focusing on deterministic methods of solving kinetic equations for electrons under different conditions. We illustrate the appearance of distinct groups of electrons in the cathode region of DC discharges and discuss the physical models appropriate for each group. These kinetic models are currently being incorporated into AMAR methodology for multi-scale plasma simulations.

© 2011 Elsevier Inc. All rights reserved.

1. Introduction

Weakly ionized plasmas contain three types of species: neutral particles (including rotationally, vibrationally and electronically excited molecules and atoms), positive and negative ions, and electrons. Plasma dynamics is characterized by a wide range of scales covering gas dynamics and electromagnetics. Typical examples include plasmas produced around hypersonic bodies entering the planet's atmosphere, lightning and thunder, ion wind of corona discharges, low-pressure reactors used for modern semiconductor manufacturing, etc. For hypersonic flows, gas heating behind a shock is responsible for plasma generation. In the other cases mentioned above, external electric fields are responsible for gas breakdown, plasma generation, and plasma-induced gas dynamic effects such as gas heating, generation of sound waves, and gas flows produced by electrohydrodynamic forces.

Depending on conditions, transport of neutral and charged plasma components is best described by either atomistic (kinetic) or continuum (fluid) models. Kinetic description is much more detailed and much more expensive compared to the continuum description in terms of density, mean velocity and temperature. In many transitional regimes, continuum description is adequate for most parts of the computational domain, and kinetic models may be necessary only in localized kinetic patches. Gas dynamic examples include supersonic flows with narrow regions of strong non-equilibrium (such as shock waves, contact, shear and boundary layers, vortex structures, etc.). In plasmas, sharp gradients of parameters and large

* Corresponding author.

E-mail address: vik@cfdrcc.com (V.I. Kolobov).

electric fields are observed in sheaths, ionization fronts, streamers and sparks, etc. Sometimes, continuum description is adequate for some plasma components whereas other component(s) should be described by kinetic models. Most often, modeling of electrons requires kinetic treatment while ions and neutral species can be described by fluid models. Furthermore, different kinetic models can be used for electrons at different energies.

It is known that classical transport phenomena in gases are described by the Boltzmann kinetic equation [1]. The Velocity Distribution Function (VDF) contains detailed information about particle motion in a 6-dimensional phase space. For systems close to equilibrium the VDF is Maxwellian, and is characterized by local values of density, mean velocity and temperature. In this case, there is no need to solve the Boltzmann equation and much simpler continuum equations (Euler, Navier–Stokes, etc.) expressing conservation laws for the first few moments (density, mean velocity and temperature) can be solved. The ratio of the particle mean free path to the characteristic size of the system (called Knudsen number) is a local characteristic of non-equilibrium for simple one-component atomic gas flows [2].

Particle based methods such as Direct Simulation Monte Carlo (DSMC) or Particle-in-Cell (PIC) have been commonly used for kinetic simulations of rarefied gases and weakly collisional plasmas [3–6]. Direct numerical solutions of kinetic equations (Boltzmann, Vlasov) have been obtained using computational grid in velocity space [7–9]. This is a rapidly developing field; recent results and further references can be found in [10–13]. Hybrid codes using kinetic and fluid models for different plasma components have been developed for plasma simulations [14,15].

The focus of this paper is on adaptive kinetic-fluid modeling incorporating kinetic phenomena in selected regions of phase space where they play an important role [16,17]. The idea is to use the minimal amount of information for the efficient description of different scales. This can be accomplished using sensors detecting phase space regions where a kinetic approach (i.e. Boltzmann equation) is required. For simple gas dynamic problems, this can be realized using domain decomposition in physical space. The computational domain can be decomposed into kinetic and continuum sub-domains as discussed in [18–25]. Methods based on domain decomposition in velocity space where fast and slow particles are treated separately have also been explored [26]. In a static formulation, this methodology has been commonly used for electrons in low temperature plasmas [27,28].

Several groups have developed coupled DSMC-continuum solvers for simulations of gas flows. However, statistical noise inherent to the particle methods has been identified as an obstacle for the development of hybrid solvers [29,30]. Due to strong fluctuations of macro-parameters calculated from the DSMC, the problem of connecting kinetic and continuum regions was complicated by severe stability problems when DSMC data is handed over to a continuum solver at the interface. Quiet DSMC methods are being developed to remedy this deficiency [31] and particle based methods for both the continuum and kinetic sub-domains have been suggested [32].

Direct kinetic solvers appear to be preferable for coupling kinetic and continuum models because similar numerical techniques are used for solving both the kinetic and continuum equations. This was already demonstrated in a Unified Flow Solver (UFS), which combines Adaptive Mesh Refinement (AMR) with automatic selection of kinetic and continuum solvers in different parts of flows based on continuum breakdown criteria. This methodology called Adaptive Mesh and Algorithm Refinement (AMAR) was first introduced in [33] for DSMC/NS coupling.

The extension of the AMAR technique to plasma simulations poses new challenges due to the multitude of temporal and spatial scales typical to weakly ionized plasmas. The development of the next generation of tools with dynamically adaptive multi-scale capabilities using different models in different parts of physical or phase space is beneficial for a variety of applications. The most striking examples are streamers and spark discharges with narrow plasma channels dynamically growing at fast electron scale.

The structure of this paper is as follows: Section 2 introduces a discrete velocity model for solving kinetic equations for rarefied gases; a shock wave example is used to illustrate the method. The kinetic equations include the Boltzmann equation(s) for one component atomic gases and gas mixtures and the Wang Chang–Uhlenbeck equation for molecules with internal degrees of freedom. Section 3 contains a brief introduction to AMR techniques and UFS methodology for neutral gas flows. Section 4 reviews fluid plasma models with AMR capabilities. Starting from a minimal plasma model, we illustrate how additional physics affects the simulation results, especially in the areas where electron kinetics plays an important role. In Section 5, we introduce Eulerian solvers for plasma kinetic equations and the concept of adaptive mesh in velocity space. Section 6 describes specifics of electron kinetics in gas discharges focusing on deterministic methods of solving kinetic equations for electrons under different conditions. We illustrate the appearance of distinct groups of electrons in the cathode region of DC discharges and discuss physical models appropriate for each group. These models are being incorporated into future AMAR methodology for multi-scale plasma simulations.

2. Discrete velocity method for solving kinetic equations

Kinetic equations are widely used in the field of rarefied gas dynamics. Kinetic description of a one-component atomic gas is based on the Boltzmann equation for a velocity distribution function, f , in a six-dimensional phase space:

$$\frac{\partial f}{\partial t} + \nabla_{\mathbf{r}} \cdot (\xi f) = I(f, f). \quad (1)$$

Here \mathbf{r} is a position vector in physical space, ξ is the velocity vector, and t is time. The right hand side of Eq. (1) contains an integral operator describing binary collisions among particles, which has the following form:

$$I(\xi) = \int_{S^2} d\Omega \int_{R^3} (f(\xi'_1)f(\xi') - f(\xi_1)f(\xi))g\sigma(g, \chi)d\xi_1 = -v(\xi)f + \Phi. \quad (2)$$

Here v is the collision frequency, Φ is the inverse collision integral, $g = |\xi_1 - \xi|$ is the relative velocity of the colliding particles, Ω is a vector on a unit sphere S^2 in velocity space, and $d\Omega$ is an element of the area of the surface of this sphere, $\sigma(g, \chi)$ is the differential collision cross section, χ is the scattering angle, and $d\xi = d\xi_x d\xi_y d\xi_z$. The post-collision velocities (ξ', ξ'_1) and the pre-collision velocities (ξ, ξ_1) satisfy the momentum and energy conservation laws.

$$\begin{aligned} \xi + \xi_1 &= \xi' + \xi'_1, \\ |\xi|^2 + |\xi_1|^2 &= |\xi'|^2 + |\xi'_1|^2. \end{aligned} \quad (3)$$

The integral (2) can also be written in the form

$$I(\xi) = \int_0^{2\pi} d\epsilon \int_0^{b_m} db \int_{R^3} (f(\xi'_1)f(\xi') - f(\xi_1)f(\xi))gb d\xi_1, \quad (4)$$

where b is the distance of the closest approach of the trajectories usually bound by a certain value b_m , and ϵ is the azimuth impact angle. The scattering angle $\chi(g, b)$ depends on the scattering potential of inter-atomic interactions. For the Hard Sphere (HS) molecules of diameter d , the scattering is isotropic, and $b = ds \sin \theta$, where $\theta = (\pi - \chi)/2$. For other commonly used scattering potentials, these relationships can be found in [34].

To solve the Boltzmann equation by a Discrete Velocity Method (DVM), a computational mesh in velocity space is introduced with nodes ξ_i . The velocity domain is selected in such a way that the VDF is negligible outside of the selected domain. Using this velocity mesh, Eq. (1) is reduced to a system of linear hyperbolic transport equations in physical space with a non-linear source term:

$$\frac{\partial f_i}{\partial t} + \nabla_{\mathbf{r}} \cdot (\xi_i f_i) = I(f_i, f_i). \quad (5)$$

For a general 3D case, the typical number of cells in velocity space, N_0 , is of the order of 10^3 . This distinguishes DVM from the Broadwell models and Lattice Boltzmann Methods, [35] which operate with much smaller number of nodes in velocity space. The DVM is similar to the Discrete Ordinate Method (DOM), which has been used for the numerical solution of the radiation transport equation.

Introducing a computational grid in physical space, one can split the solution of Eq. (5) into two stages: collisionless flow and relaxation. The collisionless flow portion can be solved by standard numerical methods for hyperbolic systems. Using an explicit finite volume numerical scheme, one obtains:

$$V \frac{f_{ij}^{*k} - f_{ij}^{k-1}}{\Delta t} + \sum_{face} (\xi_i \cdot \mathbf{n})_{face} f_{i,face}^{k-1} S_{face} = 0. \quad (6)$$

Here, index j denotes the cell number in physical space, k is the time index, $*$ denotes the intermediate time level, $f_{i,face}^{k-1}$ is the value of the function on the cell face, \mathbf{n} is the unit outward normal vector to the face, V is the cell volume, and S_{face} is the face surface area. For calculation of the face values of the distribution function, standard interpolation schemes can be used. Boundary conditions at the surface of solid objects should be defined for the VDF of the reflected particles as a sum of diffuse and specular reflections with an accommodation coefficient.

The relaxation stage has the form:

$$\frac{f_{ij}^k - f_{ij}^{*k}}{\Delta t} = -v_{ij}^{*k} f_{ij}^{*k} + \Phi_{ij}^{*k}. \quad (7)$$

Using an explicit scheme poses a restriction for the time step $\Delta t = \min(\Delta t_{adv}, \Delta t_{col})$ where $\Delta t_{adv} = h/|\xi_{max}|$ and $\Delta t_{col} = 1/v_{max}$. Here $|\xi_{max}|$ is the absolute value of the maximum particle velocity, v_{max} is the maximum value of the collision frequency. For transient problems, the time step should be selected as the minimal time step for the entire computational domain.

Computing the Boltzmann collision integral represents a challenge with respect to efficiency and precision. The discrete analog of the collision integral should (i) vanish for a Maxwellian distribution, (ii) ensure positive value of the distribution function, and (iii) satisfy conservation laws for the collision invariants (mass, momentum, and energy) in each collision, $\psi(\xi) = (1, \xi, \xi^2)$

$$\int_{R^3} \psi I(f, f) d\xi = 0. \quad (8)$$

Elastic collisions among particles of equal mass correspond to a rotation of the relative velocity vector \mathbf{g} about the center of mass. All possible outcomes lie on a 3D collision sphere with center $\xi_0 = (\xi_i + \xi_j)/2$ and radius $|g|/2$ wrapped around pre-collision velocities (see Fig. 1). Only a small number of post-collisional velocities fall exactly into the nodes of the discrete

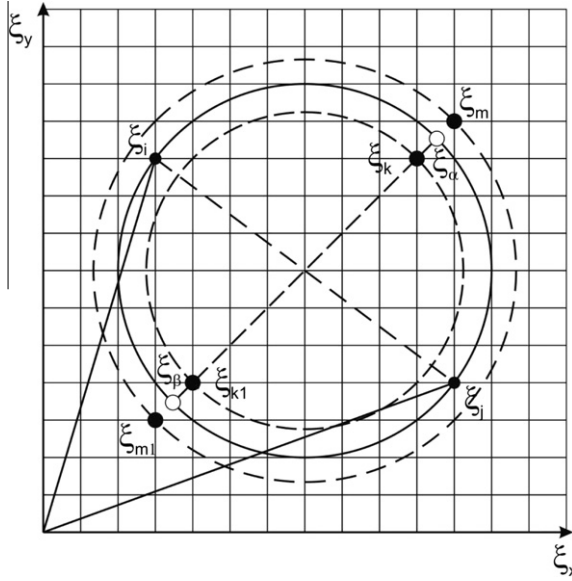


Fig. 1. Collision sphere in the (ξ_x, ξ_y) plane. ξ_i and ξ_j are pre-collision velocity nodes. Points denote post-collision velocity nodes.

velocity grid. For these points, all properties (i–iii) are satisfied automatically. To account for contributions of collisions with arbitrary orientation of the post-collision velocity vector, one has to map those points back to the grid. The mapping procedure should satisfy the conditions (i–iii).

To map an arbitrary post-collision velocity vector back to the grid, Tcheremissine [8] proposed to use the nearest integer nodes ξ_k , ξ_m (see Fig. 1). Two additional nodes ξ_{k1} , ξ_{m1} were selected symmetrically with respect to the nodes ξ_k , ξ_m to ensure conservation of mass and momentum. To enforce energy conservation in each collision and satisfy the condition $\psi(\xi_i) + \psi(\xi_j) = \psi(\xi_\alpha) + \psi(\xi_\beta)$, the value of $\psi(\xi_\alpha) + \psi(\xi_\beta)$ was interpolated using the following relation:

$$\psi(\xi_\alpha) + \psi(\xi_\beta) = (1 - r)(\psi(\xi_m) + \psi(\xi_{m1})) + r(\psi(\xi_k) + \psi(\xi_{k1})). \quad (9)$$

On a uniform grid, it is possible to perform this interpolation with one coefficient for five scalar invariant functions of the vector ψ . The coefficient r is found from the energy conservation law:

$$\xi_\alpha^2 + \xi_\beta^2 = (1 - r)(\xi_m^2 + \xi_{m1}^2) + r(\xi_k^2 + \xi_{k1}^2). \quad (10)$$

The weight coefficients r and $1 - r$ define the contributions to the closest integer nodes ξ_k , ξ_{k1} , ξ_m , ξ_{m1} (see Fig. 1). An interpolation is required for VDF calculation in these nodes, but this interpolation does not affect the conservation laws. The interpolation

$$f'_\alpha f'_\beta = (f_k f_{k1})^{1-r} (f_m f_{m1})^r, \quad (11)$$

ensures that the collision integral I vanishes for the Maxwellian distribution function.

Straightforward summation over all velocity nodes requires $O(n_a N_0^2)$ operations, where $n_a \sim O(N_0^{1/3})$ is the number of points used for integration over impact parameters, ε and b . To reduce the number of operations, one can select collision events with a Monte Carlo method or use special sequences such as Korobov nodes [36]. To further maximize efficiency, importance sampling can be used to select velocity pairs that are more likely to participate in a collision similar to DSMC selection of collision pairs [37].

Boltzmann solvers are ideally suited for parallel computations. Both the free streaming and relaxation steps involve intrinsically parallel operations: the transport in physical space involves solving N_0 independent transport Eq. (5); for collisional relaxation in velocity space, one has to solve N_r independent relaxation Eq. (7), where N_r is the number of nodes in physical space. The Graphics Processing Units (GPUs) have been recently used to solve Boltzmann equations, and impressive speedups by two orders of magnitude have been demonstrated [38,39].

2.1. Shock wave structure

To illustrate peculiarities of the DVM Boltzmann solver, consider the problem of shock wave structure. Shock wave describes collisional mixing of two equilibrium distributions with very different temperatures and mean velocities over a short distance of the order of several mean free paths [40]. For a one-component monatomic gas, the VDFs upstream and downstream of the shock are defined as two Maxwellians with densities, temperatures, and mean velocities given by the

Rankine–Hugoniot relations. Using dimensionless units with velocities normalized to the thermal velocity $v_{th} = (2kT/m)^{1/2}$, and the spatial scale in units of the mean free path λ , the computational domain in velocity space is selected as follows. The upper bound of the ξ_x velocity component, ξ_x^+ , is equal to the maximum of two quantities, $u_1 + 3\sqrt{T_1}$ and $u_2 + 3\sqrt{T_2}$, where indexes 1 and 2 denote upstream and downstream values, correspondingly. The lower bound of the ξ_x velocity component, ξ_x^- , is defined as $u_2 - 3\sqrt{T_2}$. The ξ_y and ξ_z velocity bounds are from $-3\sqrt{T_2}$ to $3\sqrt{T_2}$. The velocity cell size is usually chosen as $\Delta\xi = \sqrt{T_1}/2$. We assume that $n_1 = 1$, $T_1 = 1$, $u_1 = M\sqrt{5/6}$, where M is the Mach number.

Fig. 2 compares calculated longitudinal and transversal temperatures inside a shock for different models of intermolecular interactions. The temperatures T_{\parallel} and T_{\perp} are defined as:

$$T_{\parallel} = \frac{\int(\xi_x - u)^2 f d\xi}{\int f d\xi}; \quad T_{\perp} = \frac{\int((\xi_y - v)^2 + (\xi_z - w)^2) f d\xi}{\int f d\xi} \quad (12)$$

and normalized to the downstream temperature T_2 . As expected, the HS model yields the smallest shock thickness because the hard spheres are the most efficient scatterers [41].

With increasing Mach number, the computations become increasingly expensive because the size of velocity mesh increases rapidly. Since upstream and downstream velocity distributions have vastly different mean velocities and temperatures, coarsening velocity mesh is not possible because the mesh resolution is dictated by the lowest temperature. Using adaptive non-uniform mesh appears to be very attractive for such problems. Attempts to use non-uniform grids in velocity space have been reported [42,43]. Although there is no conceptual difficulty in attributing to each point in \mathbf{r} -space a ξ -space Cartesian grid adapted to local velocity and temperature, calculation of Boltzmann collision integral on such a grid poses considerable difficulties. Using multi-level methods with different resolutions in velocity space for transport and collision steps appear to be beneficial. It might be convenient to use more points in velocity space during the transport step because the collision step is more expensive and more accurate [41].

2.2. Gas mixtures

For mixtures of atomic gases, one has to solve a set of Boltzmann equations for each component. For the shock structure simulations with DVM, this was done in a number of publications (see [44–46] and references therein). The structure of the shock wave depends on the relative mass ratio of the components, their collision diameters, and relative mass fraction of the components. It is convenient to use momentum space rather than velocity space for calculations of the collision integral.

Fig. 3 shows the distribution of normalized densities $[(n_i(x) - n_{i-})/(n_{i+} - n_{i-})]$ and temperatures of gas species for a shock wave at $M = 2$ in a binary mixture with mass ratio 1/4, and the upstream density of heavy component 0.9. The HS model is used with equal molecular diameters. The heavy component reacts to the shock with a delay compared to the light component. The temperature of the heavy component is not monotonic, an “overshoot” is observed for certain conditions.

Fig. 4 shows the velocity distribution functions (averaged over y - and z -directions) of both species at different locations inside the shock using common momentum space. It should be noted that with increasing the mass ratio, the computational time increases sharply. However, for a gas mixture with a large difference of mass between the components, the collision integral can be substantially simplified [47].

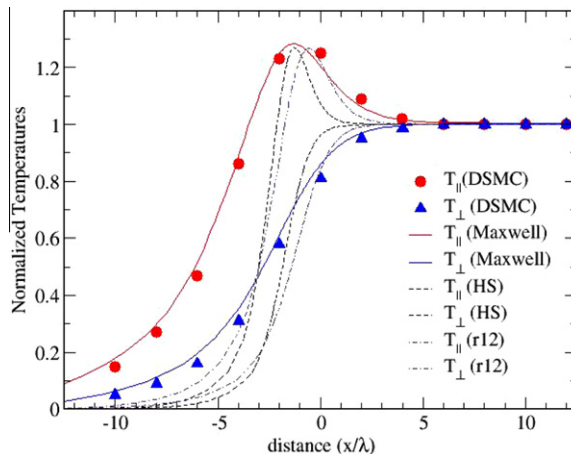


Fig. 2. Comparison of normalized longitudinal and transversal temperatures, T_{\parallel}/T_2 and T_{\perp}/T_2 , for different models of intermolecular interactions for a shock wave at $M = 5$. Maxwell model (solid line), HS model (dashed line), and inverse power of 12 model (dash-dot line). Symbols denote DSMC results for Maxwell molecules.

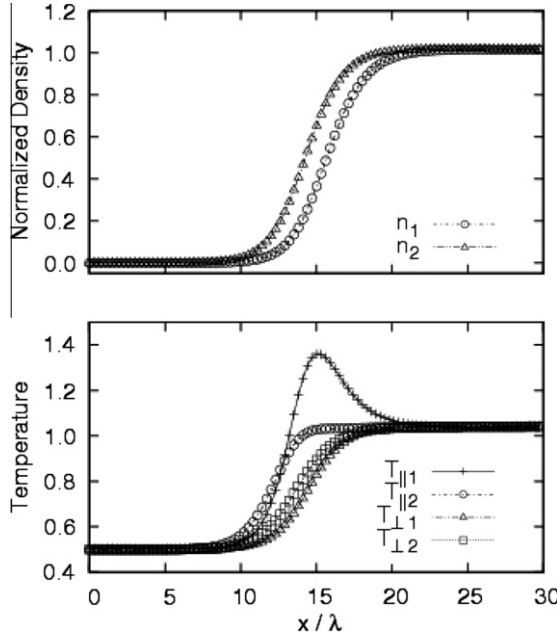


Fig. 3. Profiles of normalized species density, and parallel and perpendicular temperatures for the shock wave in a binary gas mixture for $M = 2$ and $m_1/m_2 = 1/4$.

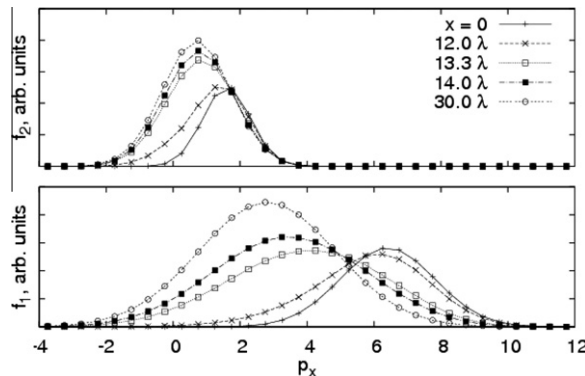


Fig. 4. Velocity distributions of light (top) and heavy (bottom) species at different points of the shock wave for $M = 2$ and mass ratio $1/4$. The species momentum space p_x is used as x -axis.

2.3. Internal degrees of freedom

Kinetic description of molecules with internal degrees of freedom is based on the Wang–Chang–Uhlenbeck (WCU) kinetic equations:

$$\frac{\partial f_i}{\partial t} + \nabla_r \cdot (\xi_i f_i) = \sum_{j,k,l} \int_{R^3} \int_{S^2} (f_k f_l - f_j f_i) g \sigma_{ij}^{kl} d\Omega. \quad (13)$$

Here, index i corresponds to quantum numbers for the internal state of the molecule, ξ_i is the velocity of the molecule in the i th state, indices i, j and k, l correspond to the molecular states before and after the collision, respectively; σ_{ij}^{kl} is the cross section for the collision responsible for this change of the internal states.

A WCU solver was developed by Tcheremissine [48] as an extension of the Boltzmann solver for inelastic collisions. This WCU solver was demonstrated for simulations of the shock wave structure in Nitrogen over a range of Mach numbers [49]. The number of rotational levels was selected based on Mach number and the temperature range of the problem. Fig. 5 shows distributions of gas density, translational and rotational temperatures obtained for $M = 13$. These results are in agreement with the experimental data and computations by DSMC method [50].

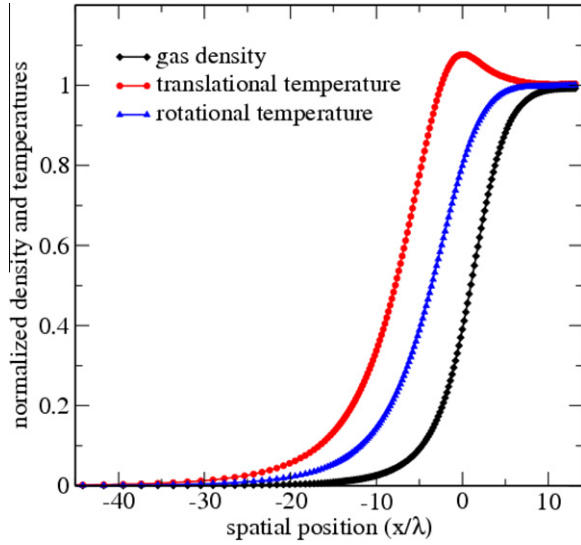


Fig. 5. Shock wave structure in Nitrogen at $M = 12.9$.

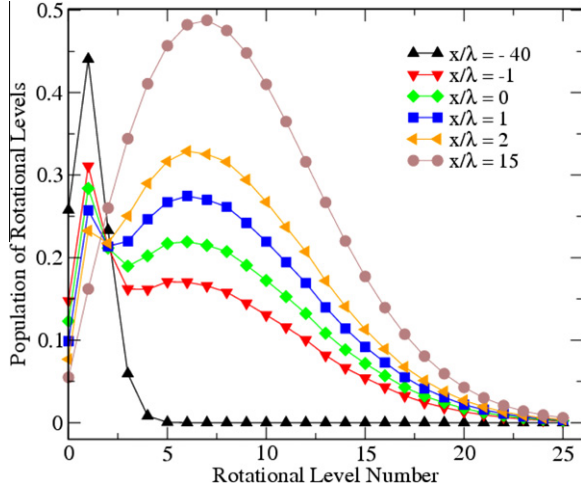


Fig. 6. Rotational spectra at different points along the shock in Nitrogen at $M = 13$.

Fig. 6 shows the rotational spectrum for 25 levels at several points along the shock for $M = 13$. The center of shock is located at $x = 0$. It is clearly seen that the rotational equilibrium inside the shock does not exist for this high Mach number.

The WCU model for rotationally excited molecules is rather expensive computationally because a separate kinetic equation is solved for each rotational level of the molecule. For practical applications, simplified models [51] might be sufficient. Simultaneous account for vibrational and rotational non-equilibrium based on a state-to-state kinetic description is not really necessary because the characteristic energies and time scales for the rotational and vibrational excitation processes are quite different. Usually, vibrational equilibration occurs considerably slower compared to the translational and rotational equilibration. As a result, in most cases, it is adequate to use continuum models in the computational domains where vibrational relaxation takes place.

2.4. Chemical reactions

Kinetic description of chemical reactions can be done on the basis of Boltzmann-like kinetic equations for a gas mixture taking into account the transfer of mass and energy in chemical interactions. However, practical simulations are rather cumbersome and have not been done so far. Recent paper [52] suggests an extension of the BGK approach to chemical reactions and shows the shock wave structure in reactive gas mixtures calculated with DVM. In many practical problems, chemical reactions are slow compared to elastic collisions, and a continuum description can be applied in the regions where chemical reactions are important (such as the area behind a strong shock [53]).

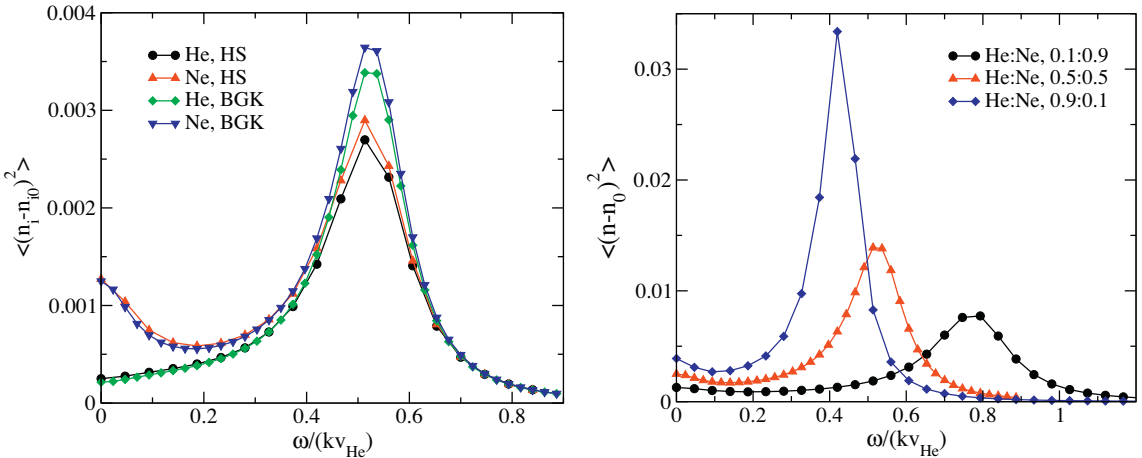


Fig. 7. Density modulation of different species in a HeNe mixture with 0.5:0.5 mass fractions obtained with BGK and HS models (left). Total density modulation according to BGK model for different mass fraction of species at $\text{Kn} = 0.01$ (right).

2.5. Forces

Spatially periodic perturbations of gas density under the effect of crossed laser beams (optical lattices) have been recently studied for several applications [54]. DVM has been applied for analysis of optical lattices to solve a set of kinetic equations in the form: [55]

$$\left(\xi - \frac{\omega}{k}\right) \frac{\partial f_\alpha}{\partial \xi} + F_\alpha(x) \frac{\partial f_\alpha}{\partial \xi} = J_\alpha. \quad (14)$$

These equations describe VDFs of gas species formed by a periodic force, $F(x) = F_0 \sin(kx)$ induced by a traveling electromagnetic wave with angular frequency ω and a wave vector k . The kinetic equations were solved at $0 < kx < 2\pi$ using cyclic boundary conditions at $x = 0$ and $x = 2\pi/k$, for different values of the angular frequency, ω , Knudsen number, and gas composition. Fig. 7 (left part) shows the calculated density modulation of species in a HeNe mixture obtained with HS and BGK models. The observed resonance corresponds to optimal conditions for sound wave propagation in the binary gas mixture. The right part of Fig. 7 illustrates the influence of gas composition on density perturbations, reflecting changes in sound speed for gas mixtures with different composition.

3. Multi-scale gas dynamics and Unified Flow Solver

Unified Flow Solver combines AMR techniques with automatic selection of kinetic and fluid models for multi-scale simulations of gas flows in transitional regimes [56]. Kinetic solvers are based on DVM described above. In this section, we introduce AMR and UFS methodologies, give some details about continuum flow solvers with Cartesian mesh, and briefly describe criteria for domain decomposition and coupling algorithms for neutral gases.

3.1. Adaptive mesh refinement

AMR is crucial for efficient solutions of multi-scale problems characterized by sharp gradients of parameters in localized areas of computational domain. Most AMR methods have been developed for finite element solvers on unstructured grids. They provide geometric flexibility at a cost of explicitly storing neighborhood relations between mesh elements. These mainly tetrahedral-based methods often fail to maintain element quality during mesh coarsening and refinement. Block-structured AMRs use unions of regular structured grid. They offer an easy route for adding AMR capabilities to existing codes with a logically Cartesian structured mesh. In a cell-based AMR, each node represents an individual grid cell. The cell-based AMR provides the greatest flexibility for local mesh adaptation offering better control for grid resolution and computational efficiency. Tree-based mesh generation methods strike a balance between simplicity and adaptivity for mesh generation. Trees are hierarchical data structures, which have been used for over three decades for efficient searching of large data sets, visualization, and mesh generation [57]. Currently, tree-based methods are being developed for extreme large scale AMR simulations with billions of cells [58]. Many AMR codes have been developed for large-scale computations in astrophysics [59].

The open source Gerris Flow Solver (GFS) [60] is used as a framework for UFS. GFS uses an octree-based mesh generation method for 3D computations. An octree is a tree data structure in which every node has a maximum of eight children.

Octrees are analogous to binary trees (maximum of two children per node) in one dimension and quad-tree (maximum of four children per node) in two dimensions. A node with no children is called a leaf and a node with no parent is called a root. All other interior nodes have exactly one parent. The depth of a node from the root is referred to as its level, with the root having level 0 (see Fig. 8).

The computational grid can be generated by subsequent division of square boxes into smaller boxes with linear dimensions equal to half of the initial dimension (left part of Fig. 8). This procedure of creating the computational mesh can be represented by a tree (the right part of Fig. 8). The root of the tree (0th level) corresponds to initial cube, the first level corresponds to 4 (in 2D) or 8 (in 3D) cubes obtained by division of the initial cube, etc. The computational cells correspond to leaves of the tree. The order of cell traversing is shown in Fig. 8 by dashed lines with arrows. All computation procedures are called only for the leaves of the tree. The 2-to-1 balance condition, where the lengths or face-neighboring cells may differ by at most a factor of 2, ensures smooth gradation in mesh size and simplifies interpolation procedures.

To perform computations only for a part of the domain (for instance, the sub-domain shown by the blue color in Fig. 9), one introduces a flag for each leaf to identify whether or not the cell belongs to the selected sub-domain. After introducing flags, the procedure of cell traversing is modified to visit only the cells belonging to the selected sub-domain. As shown on the right part of Fig. 9, only the branches connected by solid lines are traversed. To specify boundary conditions, ghost cells (hatched in Fig. 9) are used. The branches corresponding to the ghost cells are shown by dashed lines on the graph. The ghost cells are marked using a different flag, and can be traversed separately by the code.

For parallel computations, Space Filling Curves (SFC) [61,62] provide an efficient tool for domain decomposition among processors. During sequential traversing of the cells by natural order, the physical space is filled with curves in Morton order (shown in left part of Fig. 10). After this ordering of cells, all cells can be considered as a one-dimensional array. Different weights can be assigned to each cell proportional to the CPU time required to perform computations in this cell. Furthermore, the array modified with corresponding weights is subdivided into sub-arrays equal to the number of processors, in such a way that the weights of the sub-arrays are approximately the same (right part of Fig. 10). This method allows complete flexibility for a fine-grained domain decomposition with highly efficient dynamic load balancing among processors.

GFS uses coarse-grained domain decomposition for parallel computations where an entire quad/octree becomes the smallest parallel subdomain [63]. For parallel computations, the computational domain is tiled using multiple octrees (a “forest of octrees”) connected through their common boundaries. Graph partitioning algorithms are used for domain decomposition and dynamic load balancing. A discussion of advantages and drawbacks of the coarse-grained and fine-grained parallelism can be found in [63]. The SFC method was used for parallel simulations in UFS, the “forest of octrees” was used for parallel plasma simulations described below.

In a conventional octree representation, such as used in PARAMESH, the connectivity information between an individual cell and its neighbors needs to be stored explicitly, which requires 19 words of computer memory to maintain the octree data structure. In the fully threaded tree (FTT) all cells are organized into groups called octs [64]. Each oct stores pointers to eight child cells and to a parent cell, requiring $2\frac{3}{8}$ words per cell. FTT significantly reduces the memory usage and facilitates rapid search for cell neighbors compared to the worst case scenario where finding a neighbor cell implies going all the way up to the tree root and then down again. GFS has a built-in FTT library to find the cell position efficiently using the tree topology.

Further improvements of efficiency are possible using hash tables [65]. A unique key can be assigned to each node of the octree, and the traversal operations can be reduced to key manipulations performed in local memory. The pointerless representation of octrees is becoming popular due to ability to work in parallel and GPU architectures. The recently proposed data structure [66] requires only 5/8 words per cell to organize and store the AMR data for mesh connectivity. GPU-

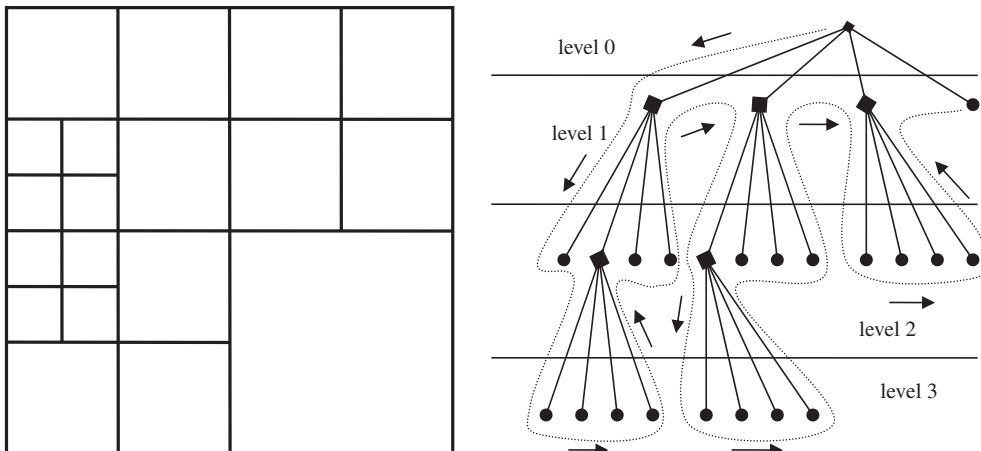


Fig. 8. Computational mesh and the tree corresponding to it.

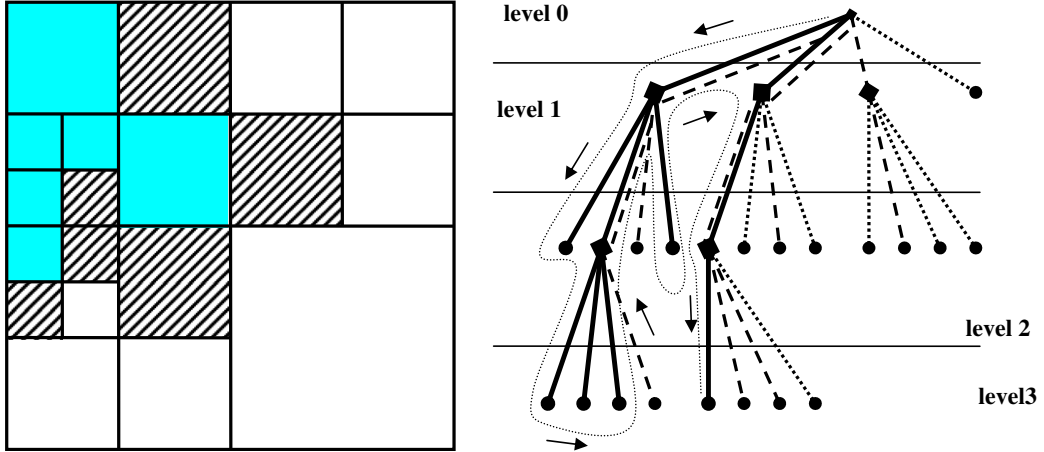


Fig. 9. The part of computational domain and the sub-tree corresponding to it.

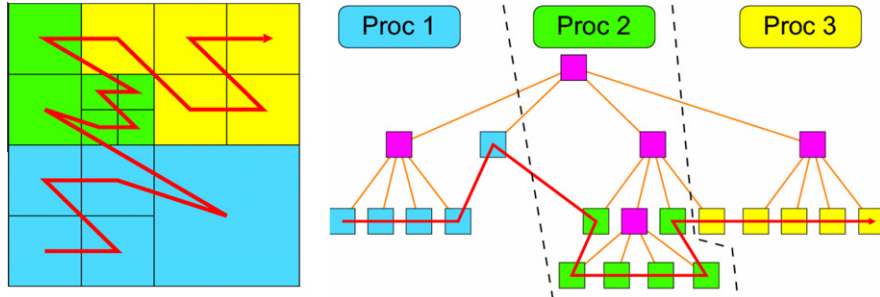


Fig. 10. Domain partitioning obtained with SFC algorithm.

acceleration of octree search can be achieved by combining the memory efficiency of hashed octree with the structure of graphics hardware [67].

3.2. Continuum flow solvers with adaptive Cartesian mesh

Traditional fluid descriptions of gas flows are based on Euler or Navier–Stokes equations. Recently, a variety of gas kinetic schemes and Lattice Boltzmann Methods have been introduced (see [68,69] and [70] for further references). These methods use the Boltzmann equation for building numerical algorithms for the continuum solvers. Continuum flow solvers with Cartesian mesh are increasingly being used for incompressible inviscid and viscous flow simulations with complex boundaries. Compressible flow solvers with AMR were developed in [71,72]. The NASCART-GT viscous Cartesian solver uses Roe scheme with MUSCL reconstruction. Originally, UFS used a gas kinetic scheme to facilitate coupling to the Boltzmann solver. Recently, a traditional scheme similar to the NASCART-GT has been added.

The Cartesian mesh approach allows automatic mesh generation with minimum user intervention and dynamic mesh adaptation to flow solution and moving bodies. The user specifies body geometry and a code automatically finds the intersection of the body surface with the Cartesian cells during the grid generation process. The main challenge of using Cartesian grids is the implementation of surface boundary conditions, since Cartesian grids, in general, are not body aligned. There are two major methods for the boundary treatment with Cartesian mesh: a cut-cell method and an Immersed Boundary Method (IBM). In the cut-cell method, boundary conditions are specified by extrapolating the solution *within* the fluid domain. The cut-cells of small size are merged with larger neighboring cells (Fig. 11). In IBM approach, ghost cells are introduced inside solids and boundary conditions on a solid surface are obtained at nodes *outside* the flow domain [73–75]. Some of the IBM methods use a “forcing” term, which is added to Navier–Stokes equations either before or after their discretization. Others use an interpolation from ghost cells to satisfy boundary conditions on the surface. The IBM is increasingly being used for simulations of viscous compressible flows with complex steady and moving boundaries (see [76,77] for further references).

The cut-cell approach is known to introduce numerical fluctuations in the predicted surface quantities [71]. Merging small cells with larger neighboring cells produces non-smooth variations of the surface cell volumes and large fluctuations of pressure, skin friction, and heat flux for the Navier–Stokes solvers with Cartesian mesh. Heat fluxes are particularly

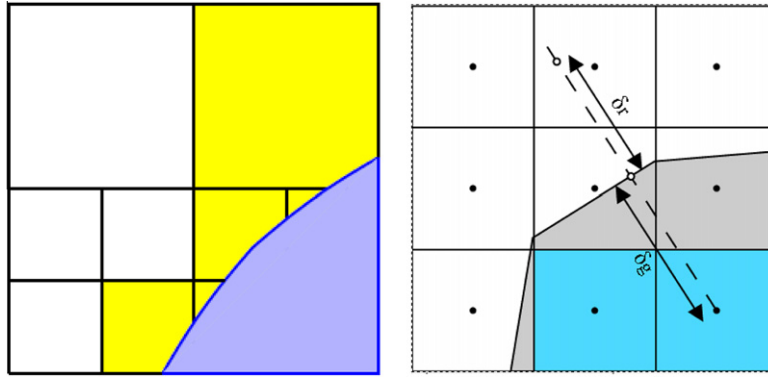


Fig. 11. Illustration of the cut-cell approach (left) and IBM approach with ghost cells (right). Cut cells are yellow on the left, ghost cells are blue on the right. (For interpretation of the references to colour in this figure legend, the reader is referred to the web version of this article.)

sensitive to boundary conditions being gradient quantities of flow properties. IBM helps to mitigate or eliminate this deficiency. Instead of directly specifying boundary conditions at a wall, primitive variables are enforced on ghost cells inside solid domains. In order to calculate the state vector in a ghost cell, a closest point to the ghost cell center at the solid panel is found and the corresponding distance δ_g is determined (see Fig. 11). Then, a reference cell is found at a distance δ_r from the surface, equal to the local cell diagonal. Using an imposed boundary condition (slip or no-slip for velocity, isothermal or adiabatic for temperature), the state vector is extrapolated from the reference cell to the ghost cell center. Cut cells shown as grey in the right part of Fig. 11 are considered as full cells [78].

Fig. 12 compares the pressure coefficient, surface friction, and heat fluxes obtained with cut-cell and IBM for gas flow around a cylinder at $M = 5$, $Kn = 0.01$. One can see that IBM predicts surface quantities that are smooth along the surface even on relatively coarse grids used for these simulations. The cut-cell results are noisy for such coarse grids; their quality can be improved by increasing the grid resolution around the solid surface, but cannot be completely eliminated. Thus, IBM allows one to completely eliminate unphysical fluctuations of skin friction and heat flux at solid boundaries for viscous flow simulations with adaptive Cartesian mesh.

3.3. Domain decomposition and coupling algorithm

The main challenge of hybrid methods is the selection of kinetic and fluid regions. The applicability of different continuum breakdown criteria depends on the type of problem being studied. For a simple one-component gas, the key parameter defining the choice of appropriate physical model is the local Knudsen number. One can use the following switching criteria:

$$S_\rho = Kn \frac{1}{\rho} |\nabla \rho|, \quad (15)$$

$$S_{NS} = Kn \sqrt{\left(\frac{\nabla p}{p}\right)^2 + \frac{1}{U^2} \left[\left(\frac{\partial u}{\partial x}\right)^2 + \left(\frac{\partial v}{\partial y}\right)^2 + \left(\frac{\partial w}{\partial z}\right)^2 \right]}, \quad (16)$$

where $U^2 = u^2 + v^2 + w^2$. It was found by experimentation that for supersonic external flows the criterion (15) correctly detects kinetic domains around the shock and behind a solid body at moderate Knudsen numbers, but predicts too small kinetic domain behind the body at small Knudsen numbers. The criterion (16) better identifies kinetic regions behind the bodies.

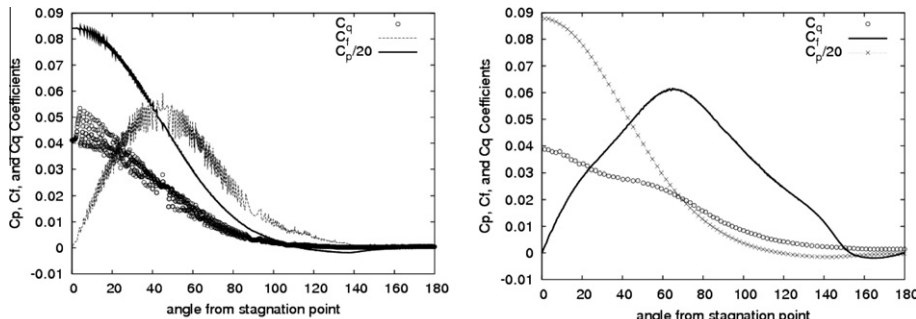


Fig. 12. Results of calculations with cut-cell (left) and IBM (right) for flow around a cylinder at $M_\infty = 5$, $Kn_\infty = 0.01$.

For coupling the Boltzmann and Euler solvers at the kinetic-fluid interface, the boundary conditions for the Euler equations are determined from the moments of the VDF in the neighbor cells. From the known VDF, parameters of the corresponding Maxwellian distribution are defined. The boundary conditions for the Boltzmann equation are obtained assuming Maxwellian VDF in the continuum cells.

For coupling the Boltzmann and N-S solvers, it is theoretically consistent to specify the velocity distribution function in fluid cells in the Chapman–Enskog form:

$$f(\mathbf{C}) = f_M(\mathbf{C}) \left(1 + q_i C_i \left(\frac{2}{5} C^2 - 1 \right) + \tau_{ij} C_i C_j \right) = f_M(\mathbf{C}) \Gamma(\mathbf{C}), \quad (17)$$

where $\mathbf{C} = (\xi - \mathbf{U}) / v_{th}$, $q_i = -\frac{\chi}{pv_{th}} \left(\frac{2m}{kT} \right)^{1/2} \frac{\partial T}{\partial x_i}$ is the dimensionless heat flux vector and $\tau_{ij} = -\frac{\mu}{p} \left(\frac{\partial u_i}{\partial x_j} + \frac{\partial u_j}{\partial x_i} - \frac{2}{3} \delta_{ij} \frac{\partial u_k}{\partial x_k} \right)$ is the dimensionless shear stress tensor. The transport coefficients (viscosity μ and thermal conductivity χ) depend on specific models of molecular interactions and should be consistent with collision models used in the kinetic solver. The Chapman–Enskog parameter Γ is a good measure of non-equilibrium conditions. When Γ is far from unity, the N-S equations are expected to fail, and the kinetic solver must be used.

For coupling the Boltzmann and N-S solvers in UFS, a continuum cell adjacent to a Boltzmann cell was identified first. In this cell, a velocity grid was introduced identical to the kinetic cell. On this velocity grid, the VDFs were constructed according to the Chapman–Enskog formula (17) or the BGK kinetic scheme. The results were consistent as long as the coupling occurred in the area where the distribution function is close to equilibrium. It was found that using fluid model in the kinetic domain could result in negative values of the VDF and incorrect computation of the flow field.

3.4. Illustration of UFS methodology

Fig. 13 shows an example of hybrid Boltzmann–Euler simulations of supersonic flow of a binary mixture over a cylinder at $M = 2$, for 3 Knudsen numbers. Two species with the mass ratio of 2 with no chemical reactions are considered. The Hard Sphere model of molecular interactions is used for the Boltzmann solver. The typical number of velocity nodes (in each direction) is 15–20 depending on the Mach number and mass ratio of gas species. The domain decomposition is performed using continuum breakdown criterion based on the gradient of the total gas density. The temperatures of species become different in the kinetic domains while they are equal in the continuum domains.

In conclusion to this section, adaptive kinetic-fluid simulations have been demonstrated for neutral gas flows using AMAR techniques. Additional research is needed to study multi-component gas mixtures and chemical reactions. Some of the challenges are described in [79]. The extent of the kinetic domain can be different for different gas species, especially for gas mixtures with large difference of mass between the components. New principal challenges appear in the presence of electric

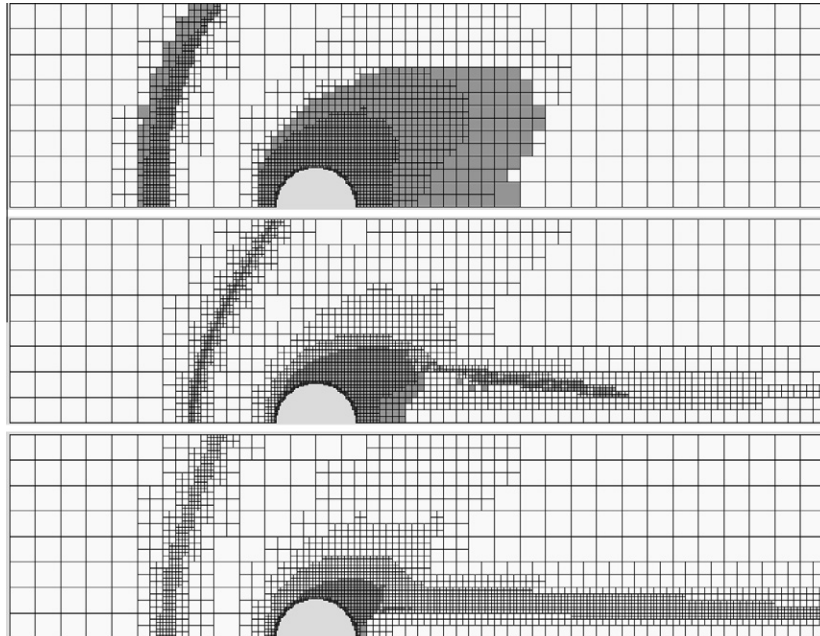


Fig. 13. The computational mesh and kinetic/continuum domains for binary mixture of monatomic gases at $M = 2$, for Kn numbers 0.125, 0.025, and 0.0125.

fields and charged particles. The disparate mass of electrons and atoms creates interesting problems for extending AMR methodology to plasma simulations.

4. Fluid plasma simulations with adaptive Cartesian mesh

Fluid models have been widely used for simulations of weakly ionized plasmas using traditional mesh techniques. These models utilize two (density and velocity) or three (density, velocity, and temperature) equations for electrons, ions and neutral species coupled to electromagnetic solvers. Fig. 14 shows an example of 3D fluid simulations of an industrial ICP source performed with CFD-ACE+ software [80]. The simulations include the solution of Maxwell equations for the electromagnetic fields produced by RF current in the coil (top part of the figure), multi-component reactive gas flow in the low-pressure chamber (Mach number is shown in the horizontal plane), and plasma generation in the chamber (electron density is shown in the vertical plane). The computational mesh was highly non-uniform to account for large gradients of plasma parameters in the narrow space-charge sheaths near the plasma boundaries. The corresponding PDEs were discretized using a Finite Volume method and solved sequentially using implicit schemes with different time steps for electron transport and heavy species transport. Recently, finite element methods (FEM) have also been used for modeling non-equilibrium plasmas and gas discharges [81,82].

4.1. Adaptive mesh refinement for plasma simulations

First attempts to apply Cartesian grid with AMR to plasma simulations were reported in [83] for 2D simulations of a low-pressure ICP reactor similar to the one shown in Fig. 15. The local grid refinement near plasma boundaries was used to resolve sheath properties. Recently, AMR has been applied to simulations of atmospheric pressure discharges with streamers, filaments, sparks, and other dynamically evolving spatial structures. 2D discharge simulations using asynchronous AMR were presented for plasma flow control [84].

Typically, streamers and sparks develop in strongly non-uniform electric fields near sharp electrodes. They propagate in a form of narrow channels with plasma density in the range 10^{13} – 10^{15} cm^{-3} . Due to high plasma conductivity in the channel, the electric field is very high near streamer tips where strong ionization by electron impact leads to further expansion of the streamer. By its nature, the streamer presents an example of strongly non-uniform, non-equilibrium, unsteady plasma which requires multi-scale analysis. The first paper utilizing dynamically adaptive mesh for 2D axi-symmetric simulations of streamers [85] used an unstructured triangular mesh and a finite element method with flux corrected transport to analyze streamer development from an initial Gaussian perturbation. A similar problem was studied later using Cartesian mesh [86].

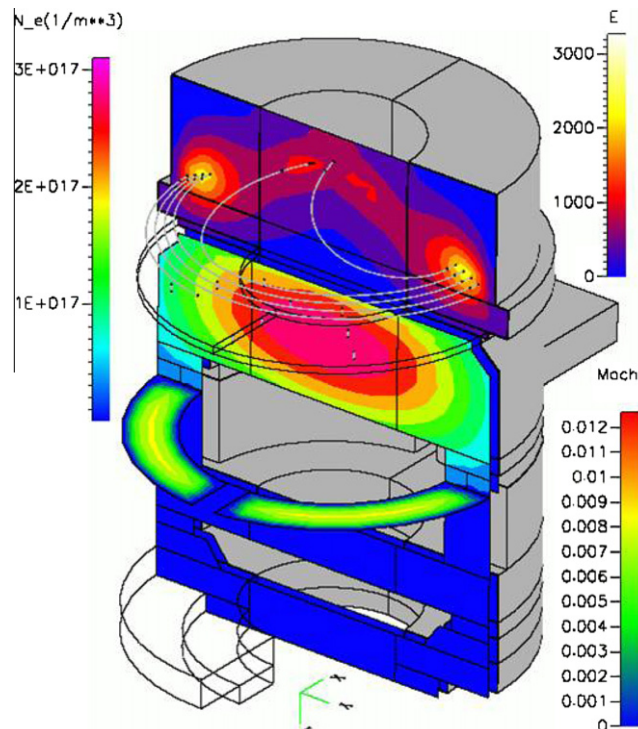


Fig. 14. 3D simulations of Panasonic Pantheon E800 Dry Etcher.

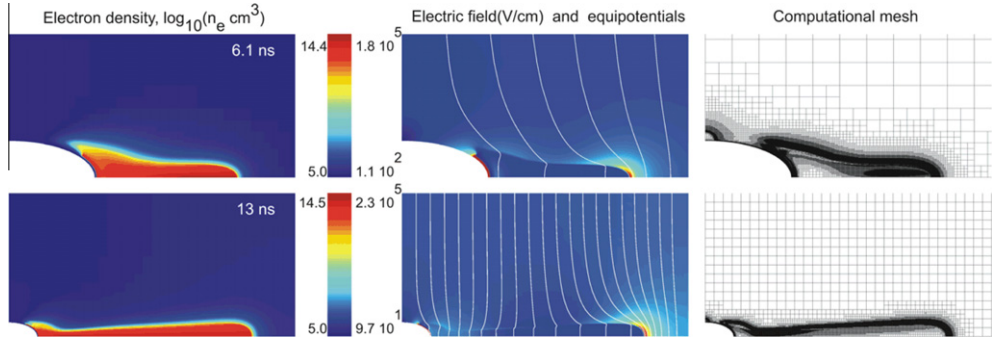


Fig. 15. 2D axi-symmetric simulation of streamer between a needle-like elliptic cathode and a flat anode: $p = 760$ Torr, voltage -600 kV, gap $d = 1$ cm.

Recently, 3D simulations of streamers with adaptive Cartesian mesh have been reported [87,88] using GFS and PARAMESH tools.

4.2. Minimal plasma model for streamer simulations

A minimal plasma model contains an equation for the electron number density, Poisson equation for the electric field, and equation(s) for ion number density assuming immobile ions. Such a model has been widely used for simulation of streamer development assuming that the ionization rate is a local function of the electric field, $v_i \sim \exp(-Bp/E)$. We have performed simulations of streamer development with AMR using dynamically adaptive quadtree/octree Cartesian mesh [87]. The equations of the minimal plasma model were solved using the finite volume method with explicit scheme for time marching. Electrode boundaries were represented using the volume-of-fluid approach of GFS. The large dynamic range of grid refinement/coarsening (up to 10–12 levels) provided high resolution of the streamer fronts. Good mesh refinement criterion was found to be important for streamer simulations. Our refinement criterion was found by experimentation in the form:

$$\alpha = 20 \left(\frac{n_e}{\max(n_e)} + \frac{n_e}{\max(n_e)} \right) + 3(\log_{10}(n_e) + \log_{10}(n_i) + \log_{10}(v_i) + \log_{10}(|E|)), \quad (18)$$

when the gradient of α exceeded a fixed value $|\nabla \alpha| > 1$ in a cell, this particular cell was refined. When $|\nabla \alpha| < 1/4$ in a cell, this cell was coarsened. The procedure of mesh refinement/coarsening was performed every 10 time steps.

Many papers have studied streamer development from an initial perturbation of plasma density in a uniform electric field. It was observed that the streamer enhances the external electric field by space charges near its tips to the values of the order of Bp , in agreement with the theory [89]. Streamers did not develop in high external electric fields (at $E > Bp$); dumb-bell shape structures appeared instead. Indeed, if the external electric field is already of the order of Bp , ionization proceeds uniformly in all directions, and narrow channels do not form.

In laboratories, streamers usually develop in corona discharges in the regions of highly non-uniform electric fields near electrodes [90,91]. Fig. 15 shows an example of 2D axi-symmetric simulations of streamer development near a needle-like cathode. A constant electron density 10^5 cm^{-3} is assumed at the cathode surface. The streamer propagates with a velocity by an order of magnitude higher than the electron drift velocity v_d in the gap. The calculated streamer velocity agrees with the classical estimate for the fast streamer velocity $v = v_i r / \ln(n_m/n_0)$, where r is the radius of the streamer tip, and n_m is the plasma density in the streamer channel.

Fig. 16 illustrates streamer development near a rod-shaped anode in corona discharge. An off-axis toroidal structure was formed in our simulations, similar to those discussed in [92]. This situation was observed in our simulations with more complicated physical models (ion transport, electron thermal conductivity) and different electrode shapes.

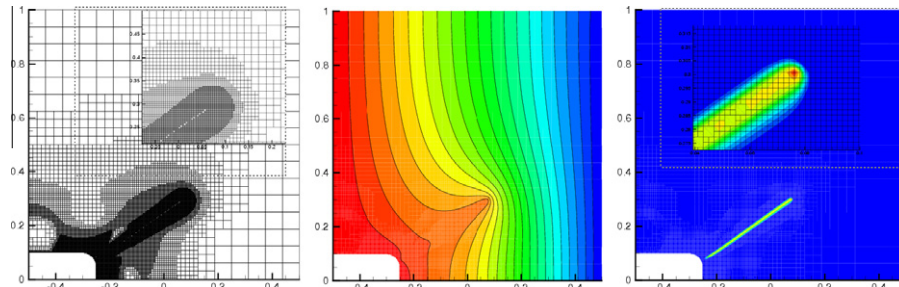


Fig. 16. The computational grid (left), electrostatic potential (center), and the electron density (right) for a streamer developing near a rod anode.

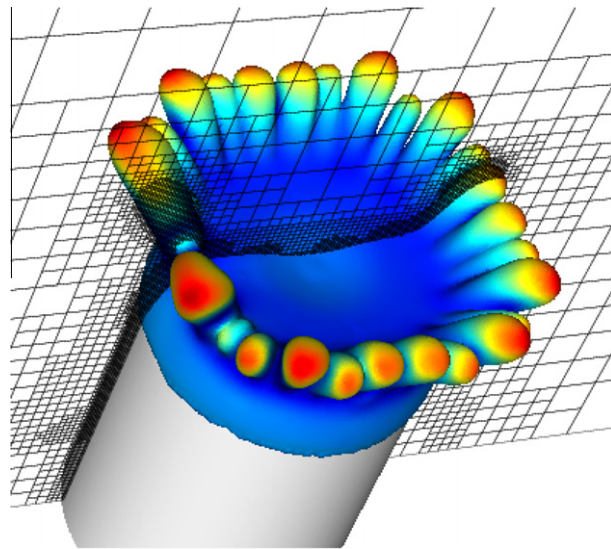


Fig. 17. Computational grid, electron density contours at 10^7 cm^{-3} , and the electric field strength (color, maximum value $7 \times 10^6 \text{ V/m}$) at 15 ns.

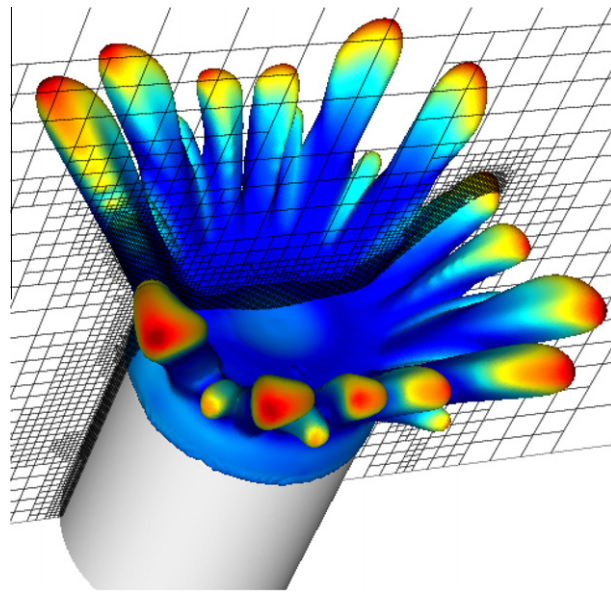


Fig. 18. Computational grid, electron density contours at 10^7 cm^{-3} , and the electric field strength (color, maximum value $7 \times 10^6 \text{ V/m}$) at 20 ns.

Parallel 3D simulations revealed that the 2D axi-symmetric channels break into separate streamers (see Figs. 17 and 18). The streamers formed near the anode surface with an almost periodic pattern and propagated in different directions with different speeds. Only two main streamers survived at a long distance from the anode. The code generates about 1.5 million cells during the simulations.

In all cases described above, the calculated fields near the streamer tips were of the order of B_p , indicating that non-local ionization should play an important role in these regions. For this reason, kinetic simulations of streamers using PIC-MCC codes [93] appear to be particularly revealing. Attempts to include nonlocal ionization, radiation transport and other potentially important physics for streamer simulations can be found in Refs [94,95]. The problem of streamer and spark discharges appears to be most suitable for application of the AMAR technique. Using the kinetic description of electrons in dynamically evolving narrow areas near the streamer tips and fluid description of plasmas in the high density channel resembles shock wave propagation in gas dynamics successfully studied by UFS.

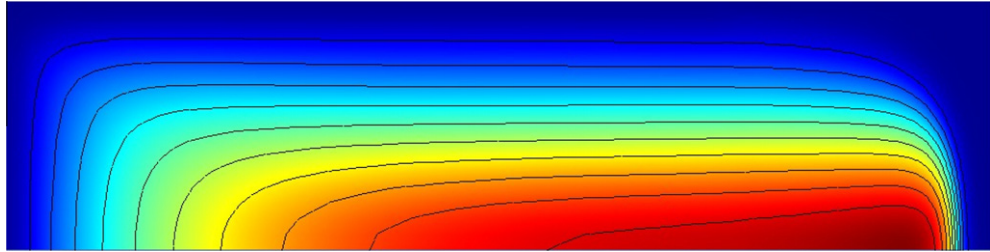


Fig. 19. Spatial distribution of electron density calculated with local ionization model.

4.3. Ion transport

By adding ion transport to the minimal plasma model, we can simulate low-pressure discharges, which are controlled by ion drift to the walls. In this section, we show the results of 2D simulations of classical DC glow discharges using such a simple model. The model accounts for ion drift, secondary electron emission from the cathode, and local ionization. We performed a series of calculations with two slightly different models. In the first model, the electron temperature was fixed to a constant value (3 eV) for calculation of the electron diffusion coefficient, and the ionization rate was assumed to be a local function of the electric field. The second model calculated the electron temperature as a function of local electric field neglecting electron thermal conductivity. This local electron temperature was used for calculation of the ionization rate and electron diffusion coefficient.

Fig. 19 shows an example of calculations for a DC glow discharge in He at a pressure of 3 Torr, tube radius $R = 1$ cm, and inter-electrode gap $L = 4$ cm. An RC external circuit is attached to the left electrode (anode) and the right electrode (cathode) is grounded. The top boundary is assumed to be a dielectric. The resistor in the external circuit, R_{ext} , was varied to change the discharge current. **Fig. 19** shows a typical structure of a glow discharge with anode and cathode sheath, and an extended region of quasi-neutral plasma. The radial structure of the discharge is controlled by electron-impact ionization and ambipolar diffusion of charged particles to the wall. The axial distribution of electric potential, electron temperature, and charged particle density shown in **Fig. 20** indicate that the cathode region turns directly into a positive column. The well-known Faraday Dark Space is completely absent according to this model.

The local field model is sufficient to demonstrate the formation of cathode spots with normal current density, and the transition from Townsend to normal discharge under discharge conditions corresponding on the right branch of the Paschen curve. **Fig. 21** demonstrates the benefits of AMR for simulation of a cage discharge generated between thin wires arranged to form a cylindrical cage. Field emission of electrons is assumed at the cathode surface.

4.4. Electron energy transport

To account for electron thermal conductivity, the electron energy transport equation was added to the plasma model. The electron energy transport equation for the electron mean energy \bar{e} is:

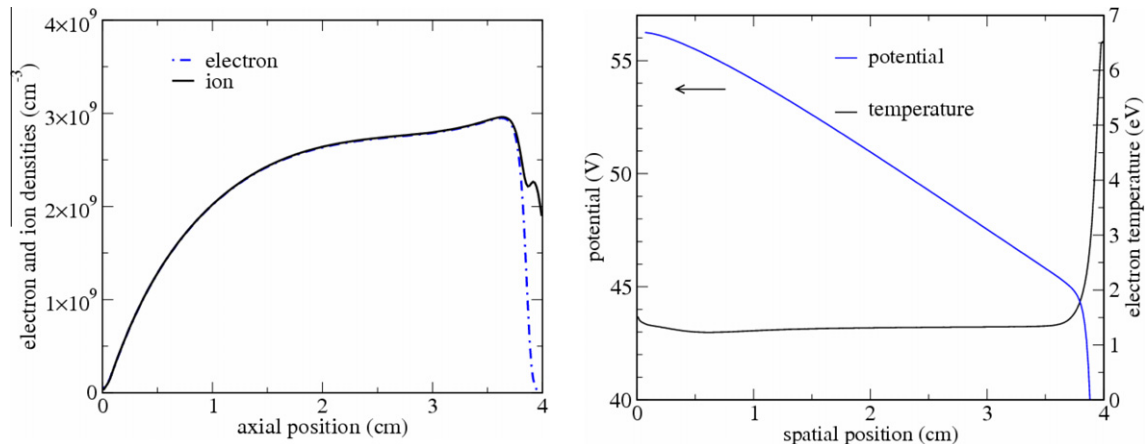


Fig. 20. Axial distributions of electron and ion densities (left), electrostatic potential and electron temperature (right) without account of electron thermal conductivity.

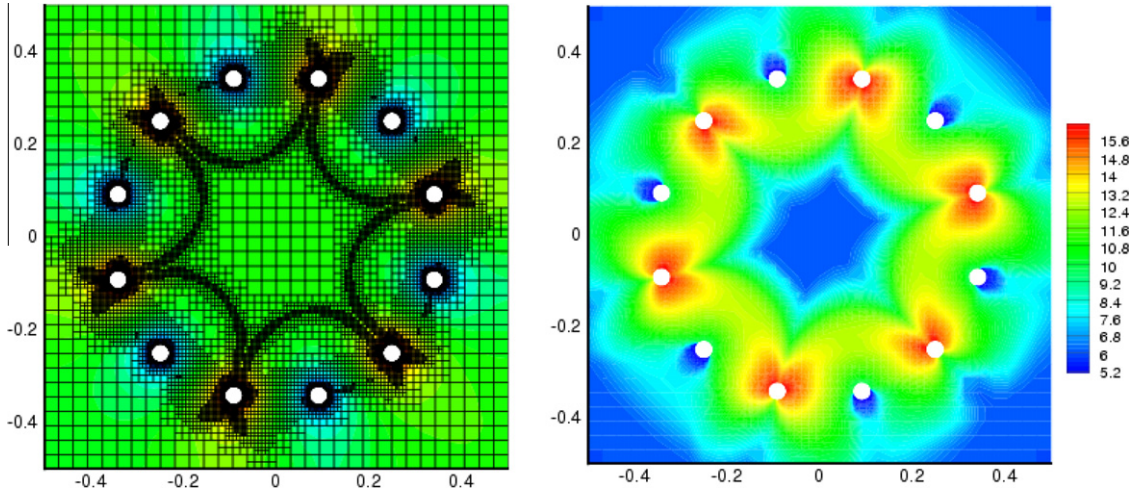


Fig. 21. Computational grid and electric potential (left), and $\log_{10}(n_e)$ (right) for a cage discharge.

$$\frac{\partial n_e}{\partial t} + \nabla \cdot \vec{\Gamma}_e = S_e, \quad (19)$$

where $n_e = n_e \bar{e}$ is the electron energy density, \bar{e} is the electron mean energy, and $\vec{\Gamma}_e$ is the electron energy flux:

$$\vec{\Gamma}_e = -\frac{5}{3}\mu_e \vec{E} n_e - \frac{5}{3}D_e \nabla n_e, \quad (20)$$

where $\mu_e(\bar{e})$ is the electron mobility, $D_e = \frac{2\mu_e \bar{e}}{3e} = \mu_e T_e$ is the diffusion coefficient, and $T_e = \frac{2\bar{e}}{3e}$ is the electron temperature.

The electron energy source term S_e was implemented in the form:

$$S_e = -e \vec{\Gamma}_e \cdot \vec{E} - n_e \sum_r \varepsilon_r k_r n_r, \quad (21)$$

where the first term represents heating by the electric field and the second term describes the energy loss in elastic and inelastic collisions of electrons with gas species.

The boundary conditions at electrodes and dielectric surfaces are

$$(\vec{\Gamma}_e \cdot \vec{n}) = -a_e \frac{5}{3}\mu_e (\vec{E} \cdot \vec{n}) n_e + \frac{2}{3}v_{th,e} n_e - \sum_p \gamma_p \bar{\varepsilon}_p (\vec{\Gamma}_p \cdot \vec{n}), \quad (22)$$

where

$$a_e = \begin{cases} 1, & -(\vec{E} \cdot \vec{n}) > 0, \\ 0, & -(\vec{E} \cdot \vec{n}) \leq 0, \end{cases} \quad (23)$$

$\bar{\varepsilon}_p$ is the mean initial energy of electrons emitted by incidence of species p (which is assumed to be 1 eV).

We have used the Scharfetter–Gummel (SG) discretization scheme for solving the electron and ion transport and for the electron energy transport. We extended the SG scheme to the octree Cartesian grid using the native GFS discretization scheme [60]. The flux at a given face of a cell was calculated as:

$$\Gamma_{face} = \frac{D_{face}}{h} (f_1(z_{face}) n_{cell} - f_2(z_{face}) n_{neighbor}), \quad (24)$$

where

$$\begin{aligned} f_1(z) &= z / (\exp(z) - 1), \\ f_2(z) &= z \exp(z) / (\exp(z) - 1) \end{aligned} \quad (25)$$

and μ_{face} , D_{face} and E_{face} are the face values of the diffusion coefficient, mobility and electric field. The quantity

$$z_{face} = \frac{\text{sgn}(q)\mu_{face}E_{face}h}{D_{face}} \quad (26)$$

is an analog of the Peclet number (q is the species charge), and n_{cell} and $n_{neighbor}$ are the values of the particle density or the electron energy at the cell center and in a neighbor cell, correspondingly. The value of $n_{neighbor}$ is calculated at the cell center of a neighbor cell if the neighbor cell is at the same refinement level as the current cell. If the neighbor cells have different

refinement levels, then $n_{neighbor}$ is calculated using a special procedure involving a set of neighbor cells, as described in [60]. The two grid points where n_{cell} and $n_{neighbor}$ are evaluated form the base points with the distance h between them. Thus calculated SG fluxes Γ_{face} are then multiplied by the face surface area, S_{face} , and summed up over all faces of the cell. In the cut (mixed) cells, a contribution of thermal fluxes at solid panels is added into this sum.

For the electron energy transport equation, special attention was paid to calculations of the Joule heating term. The inner product of the electric field and the electron current density was evaluated at the cell center as a geometrical average of the corresponding opposite face values:

$$(\vec{E} \cdot \vec{\Gamma}_e) = \frac{1}{2} \left[(\vec{E} \cdot \vec{\Gamma}_e)_{right} + (\vec{E} \cdot \vec{\Gamma}_e)_{left} + (\vec{E} \cdot \vec{\Gamma}_e)_{top} + (\vec{E} \cdot \vec{\Gamma}_e)_{bottom} + (\vec{E} \cdot \vec{\Gamma}_e)_{back} + (\vec{E} \cdot \vec{\Gamma}_e)_{front} \right]. \quad (27)$$

For the cut (mixed) cells, this averaging included the surface areas of the cut (opposite) faces and also the solid surface panels with given thermal flux boundary conditions.

Our present plasma model is explicit in time with the time step limited by several stability requirements. Coupling the electric field and electron transport (via Poisson equation) gives rise to the dielectric time limitation. This time step limitation is eliminated by using the semi-implicit Poisson equation solver. Another time step limitation arises from the CFL limit and an explicit discretization of the diffusion operator. This limitation will be tackled in the future by using an implicit scheme for electron density and electron energy transport. Finally, the time step is limited by the ionization source or chemical reactions. Depending on the plasma problem being solved (high pressure streamer discharges or low-pressure glow discharges), different stability requirements can dominate.

4.5. Effect of electron thermal conductivity

[Fig. 22](#) illustrates the effects of electron thermal conductivity on spatial distribution of plasma parameters in a classical DC glow discharge. The discharge conditions are the same as those shown above in [Fig. 19](#). The only difference is that the electron energy transport term in Eq. (18) is now accounted for.

This model reproduces qualitatively the complicated structure of the cathode region observed in experiments. In particular, the nonmonotonic distribution of the electrostatic potential is formed, which corresponds to a double layer with two field reversals in the plasma region (shown by arrows in [Fig. 23](#)). A sharp maximum of plasma density is observed in the vicinity of the first field reversal near the cathode sheath. The electron temperature reaches a minimum in the Faraday Dark Space, near the second field reversal. Careful examination and comparison with kinetic theory of the cathode region described below shows deficiencies of the fluid model, which operates with “an average electron”. Experimental observations and the kinetic theory show that the electron temperature drops in the cathode region down to the gas temperature. The fluid model cannot describe the complicated structure of the electron energy distribution function observed in the cathode region.

[Fig. 24](#) illustrates AMR capabilities for simulations for a short DC glow discharge in Argon at pressure of 3 Torr, tube radius $R = 1$ cm and inter-electrode gap $L = 1$ cm. An RC external circuit is attached to the left electrode (anode) and the right electrode (cathode) is grounded. The top boundary is assumed to be a dielectric. The grid refinement was adapted on gradients of the electric potential, normalized electron (n_e) and ion (n_i) density, as described in Eq. (18). For a discharge current of 34 μ A, we obtained a normal discharge with a well pronounced cathode spot. The radial distribution of current over the cathode surface is characterized by a sharp boundary; the current density drops sharply outside of the spot. The electron thermal conductivity is very important for the axial structure of the discharge. Due to nonlocal ionization, the electric potential forms a potential well in the plasma region. This phenomenon is more pronounced in long discharges, where a positive column is formed.

We have performed simulations of glow and corona discharges between a rod cathode and a planar anode for different gas pressures. Due to the large curvature of the cathode surface, the electric field is highly non-uniform around the cathode tip even in the absence of space charge. At the cathode surface the thermal flux conditions are assumed with a secondary electron emission coefficient $\gamma_p = 0.2$. The discharge current was changed by adjusting the resistor in the RC external circuit. For the high current regimes with large gradients of plasma parameters, the SG scheme demonstrated superior performance

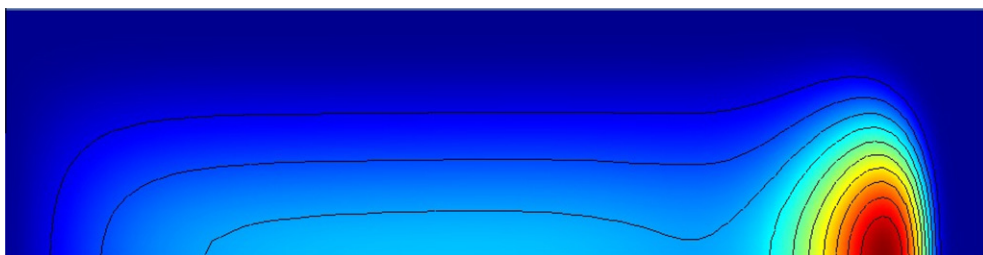


[Fig. 22](#). Spatial distribution of electron density.

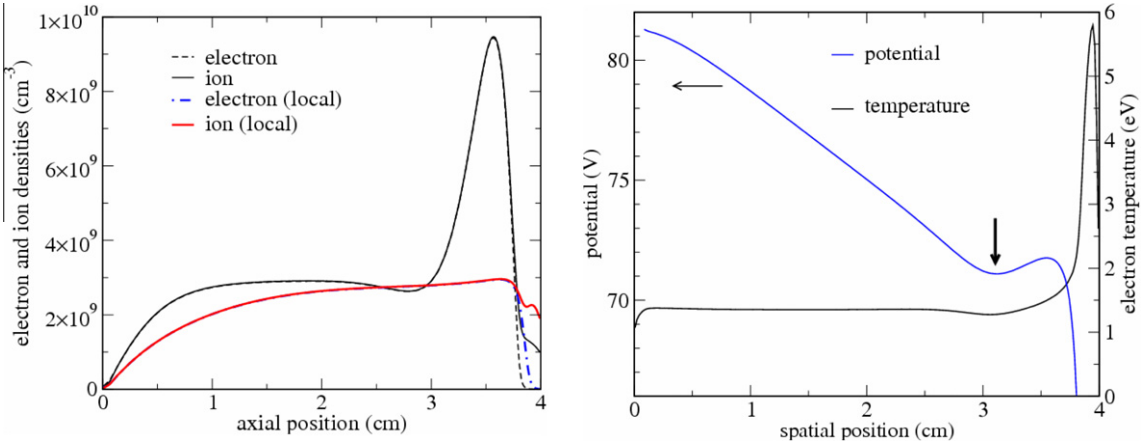


Fig. 23. Axial distributions of electron and ion densities (left), electrostatic potential and electron temperature (right) with account of electron thermal conductivity.

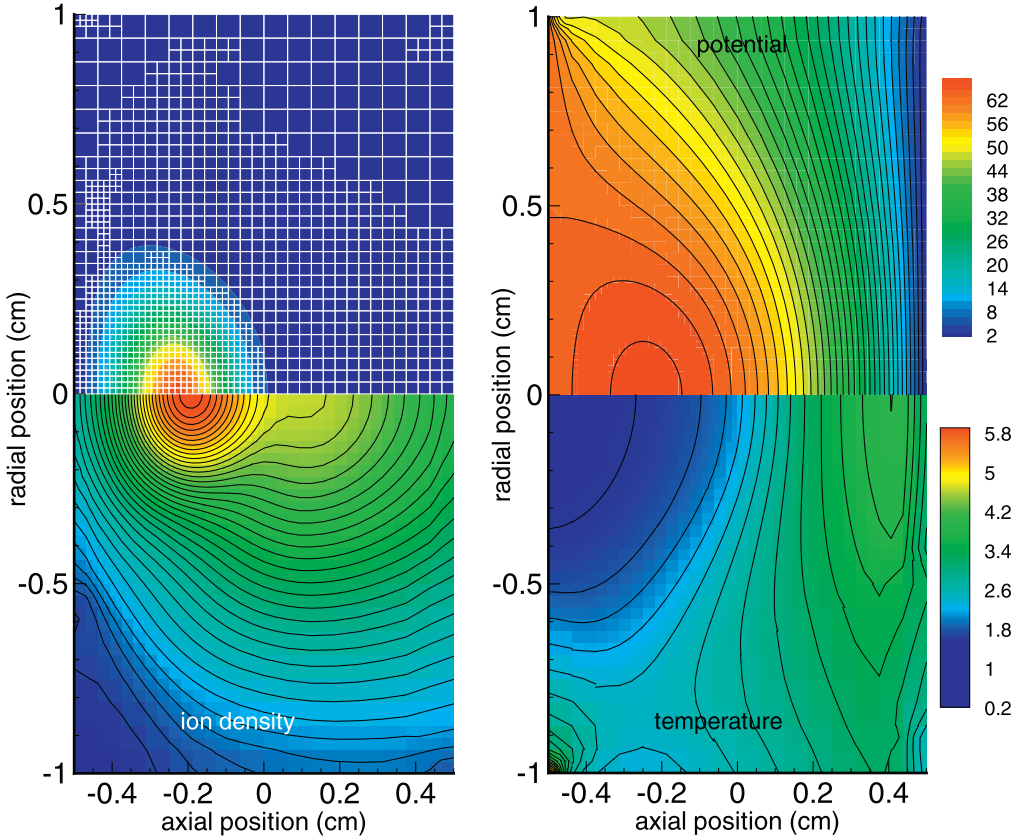


Fig. 24. Adapted grid, electric potential, electron density, ion density for simulation of a low pressure 2D DC discharge at 34 μ A (cathode to the left).

compared to other numerical schemes implemented in our code. The results for 15 Torr, 32 μ A are shown in Figs. 25 and 26. The electron temperature has a maximum of about 4 eV around the tip of the cathode, which is about half of that obtained in the 3 Torr case. The electric field is monotonic at 15 Torr and changes sign for the 3 Torr case, as in the case with the flat cathode described above.

In this section, we have shown that fluid plasma models previously developed for the traditional meshing techniques can be extended for the adaptive Cartesian mesh. We have illustrated the benefits of AMR for simulations of corona and streamer

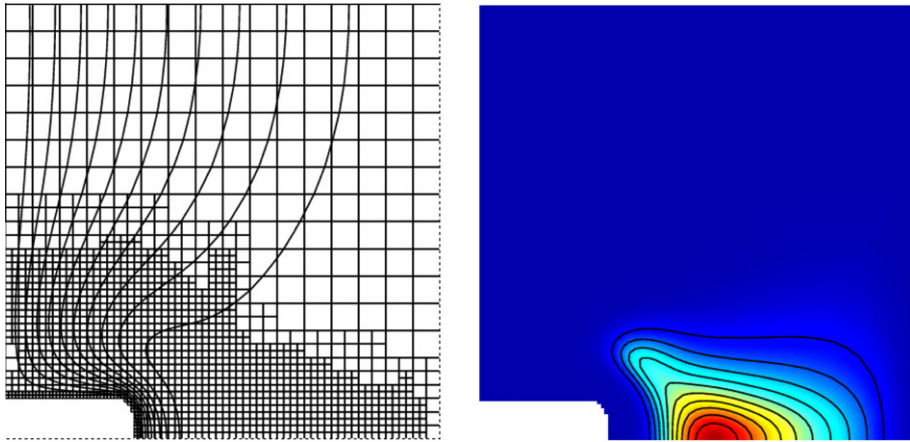


Fig. 25. Computational grid and the electrostatic potential (left), and electron density contours (right) for a glow discharge between a rod cathode and a planar anode.

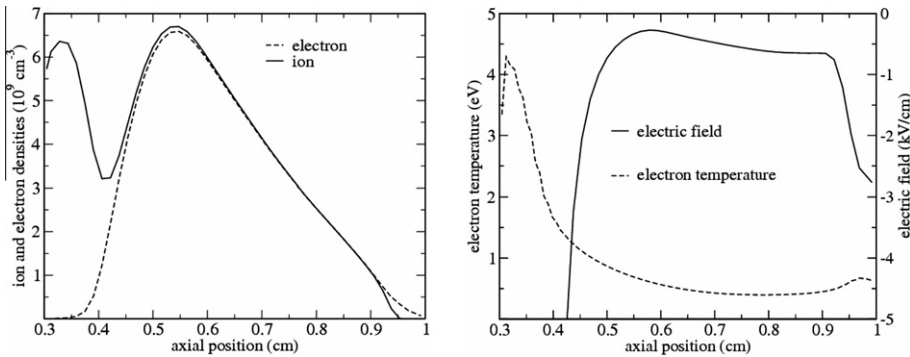


Fig. 26. The axial profiles of the electron and ion density, the electron temperature and the x -component of the electric field, E_x (zoom on the plasma region).

discharges over a wide range of gas pressures. We have also shown that fluid models can qualitatively reproduce many features of low-pressure DC glow discharges, but fail in quantitative description of details and parts of the discharges, which require kinetic treatment.

5. Eulerian solvers for plasma kinetic equations

The kinetic equation for charged particles has an additional force term due to the presence of electromagnetic fields:

$$\frac{\partial f}{\partial t} + \nabla_{\mathbf{r}} \cdot (\xi f) + \nabla_{\xi} \cdot (\mathbf{a}f) = I, \quad (28)$$

where $\mathbf{a} = e(\mathbf{E} + \xi \times \mathbf{B})/m$ is the acceleration vector due to electric and Lorentz forces. In weakly ionized plasma, the collision term in the right hand side includes large-angle Boltzmann-type collisions of charged particles with neutrals and Coulomb interactions among charged particles, which can be written in a Fokker–Planck–Landau form. In this section, we introduce Eulerian and semi-Lagrangian solvers for plasma kinetic equations.

5.1. Eulerian Vlasov solvers

The kinetic Eq. (28) without a collision term is called a Vlasov equation. The Vlasov equation expresses the invariance of the velocity distribution function along particle trajectories in phase space. The method of characteristics is the base of the Eulerian codes for the numerical solution of Vlasov equations. Below, we briefly illustrate the solution of a Vlasov–Poisson system for a 2D phase-space using cubic splines [96].

To obtain second order accuracy in time one can use operator splitting for transport in physical and velocity spaces:

$$S_\tau = A_{\tau/2} C_\tau A_{\tau/2}. \quad (29)$$

Here S_τ is the operator that transforms the solution from t to $t + \tau$, A is the operator of free streaming, $\partial f/\partial t + \xi_x \partial f/\partial x = 0$, and C is the operator of velocity transport, $\partial f/\partial t + a_x(x, t) \partial f/\partial \xi_x = 0$. In the 2D phase-space problem, the splitting reduces to the following successive shifts:

$$f^a(x, \xi_x, t + \tau/2) = f^a(x - \xi_x \tau/2, \xi_x, t), \quad (30)$$

$$f^b(x, \xi_x, t + \tau) = f^a(x, \xi_x - a_x^* \tau, t), \quad (31)$$

$$f(x, \xi_x, t + \tau/2) = f^a(x - \xi_x \tau/2, \xi_x, t). \quad (32)$$

First, a half-time shift is performed in space for each value of ξ_x . Then, the Poisson equation with charge densities calculated from the distribution functions is solved to calculate the electric field and acceleration a_x^* . This acceleration is used to calculate a shift in velocity space. Finally, another half-time shift in space is performed.

A cubic spline interpolation is used to calculate the shifted values of the distribution functions. Assuming a uniform spatial grid with nodes x_j , the shifted value of the distribution function, $f_j(x_j + \Delta) \equiv \tilde{f}_j$, is calculated from the following equation [96]

$$\tilde{f}_{j-1} + 4\tilde{f}_j + \tilde{f}_{j+1} = Af_j + Bf_j + Cf_j + Df_j, \quad (33)$$

where

$$A = (1 - \Delta)^3,$$

$$B = 4 - 3\Delta^2(2 - \Delta),$$

$$C = 4 - 3(1 - \Delta)^3(1 + \Delta),$$

$$D = \Delta^3.$$

Evidently, for $\Delta = 0$ one obtains $\tilde{f}_j = f_j$, and for $\Delta = 1$ one obtains $\tilde{f}_j = f_{j+1}$. For $0 < \Delta < 1$, the value of \tilde{f}_j is obtained from Eq. (33) by inversion of the tridiagonal matrix. These simple cubic spline interpolations on a uniform grid produce good results, as demonstrated for several cases in [96].

To illustrate the procedure outlined above, consider the problem of a collisionless DC sheath, for which an analytical solution can be obtained. Electrons and ions are injected at the right boundary ($x = d$) with Maxwellian velocity distributions. The boundary at $x = 0$ absorbs charged species and is kept at floating potential. As a result, a surface charge is built up at $x = 0$ to equalize electron and ion currents to the wall in a steady state. The problem is characterized by two parameters: the ratio of electrons to ion mass, $\delta = m/M$, and the ratio of electron to ion temperatures, $v = T_e/T_i$.

The analytical solution of the Vlasov equation for the electron velocity distribution function has the form [97]:

$$f_e(\xi, x) = \begin{cases} \exp(-\varepsilon) & \xi < \sqrt{2\Delta\varphi(x)/\delta} \\ 0 & \xi > \sqrt{2\Delta\varphi(x)/\delta}, \end{cases} \quad (34)$$

where $\varepsilon = \xi^2/2 - \varphi(x)$ is the total energy, $\varphi(x)$ is the electric potential measured in units of T_e , and $\Delta\varphi(x) = \varphi(0) - \varphi(x)$. It is assumed that $m = 1$, $\varphi(L) = 0$, and $\xi = \xi_x$. According to the analytical solution (34), the electron velocity distribution function is zero at $\xi > \sqrt{2\Delta\varphi(x)/\delta}$, because no electrons reaching the wall return back to plasma. Fig. 27 (left part) shows the results of the numerical solution of the problem. Small deviations from the analytical solution noticeable for fast electrons demonstrate the accuracy of the numerical solution. The electron density drops in the sheath because electrons are repelled by the potential well, and the electron temperature drops in a vicinity of the wall due to escape of fast electrons to the wall (see Fig. 28).

Ions are injected into the sheath with non-zero mean velocity (Bohm velocity). The ion velocity distribution function (IVDF) can be described by the analytical solution:

$$f_i(\xi, x) = \begin{cases} \exp\left(-v\left(\sqrt{\xi^2 + 2\varphi(x)} - v_0\right)^2/2\right), & \xi < 0. \\ 0 & \xi > 0, \end{cases} \quad (35)$$

It follows from this solution that the amplitude of the IVDF remains constant, and the width of $f_i(\xi, x)$ with respect to velocity decreases in the sheath. The decrease of the IVDF width corresponds to the decrease of the ion density and temperature $T_i(x)$ in the sheath (see Fig. 28). The right part of Fig. 27 shows results of the numerical solution for the DC sheath, which coincides with the analytical solution given by Eq. (35). The numerical scheme reproduces the analytical solution with remarkable accuracy.

For our numerical solutions shown above, we used dimensionless variables with space normalized to the electron Debye length r_D , time measured in units of inverse ion plasma frequency, and velocity in units of the ion acoustic speed, $c_s = \sqrt{T_e/M}$. We assumed that $L = 20$, and the ion time step was $\Delta t = 0.01$. The electron Vlasov equation and Poisson

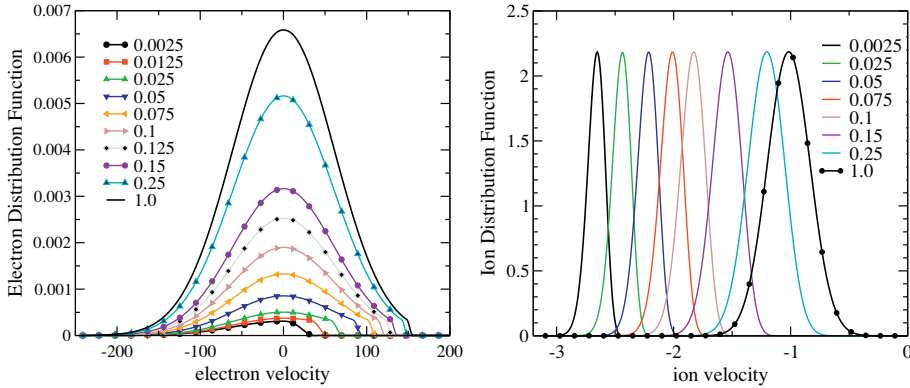


Fig. 27. Electron velocity distributions (left) and ion velocity distributions (right) at different spatial positions (x/L).

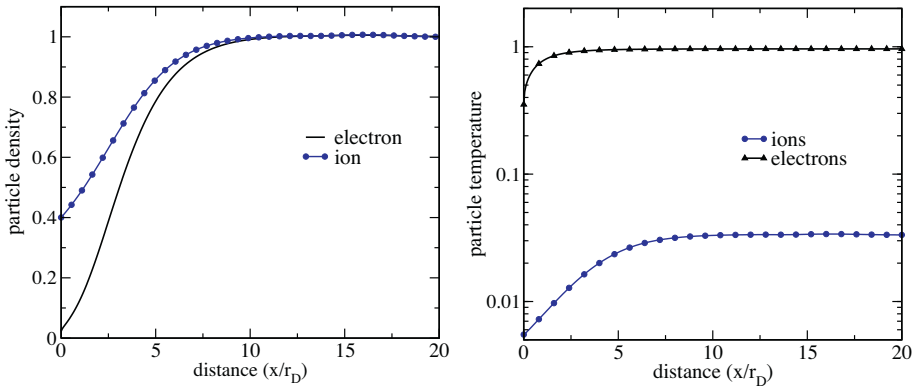


Fig. 28. Particle densities (left) and temperatures (right) for $v = 30$.

equation were solved in a sub-cycle with N_t steps, so that the electron time step was $\Delta t/N_t$ (with $N_t = 60$). The velocity range for electrons was $-4/\sqrt{\delta} < \xi_e < 4/\sqrt{\delta}$, and for ions $-17/\sqrt{v} < \xi_i < 0$. The shown results were for $v = 30$.

When the electron mean free path is comparable or larger than the characteristic size of the plasma, the electron distribution function at a point is determined not only by the local value of the electric field at this point, but also by the profile of the electric field in the vicinity of the point of size λ along the electron trajectory. As a result, the local relationship between the current density and the electric field (Ohm's law) becomes invalid. Collisionless electron heating, anomalous skin effect, non-monotonic distributions of electric and magnetic fields, and other "hot plasma" effects have been observed under these conditions [98]. With few exceptions, these phenomena have been studied so far using either semi-analytical models or PIC simulations. Eulerian Vlasov solvers appear to be quite useful for studies of low-pressure RF plasma sources operating in weakly collisional regimes.

Fig. 29 shows an example of kinetic simulations of an Inductively Coupled Plasma (ICP) with an Eulerian Vlasov code [99]. A set of Vlasov equations for electrons and ions was solved together with Maxwell equations for the inductive electric field E_y and the magnetic field B_z and Poisson equation for the electrostatic field E_x for a one-dimensional geometry. The fields, E_y and B_z decay exponentially from the plasma boundary (at $x = 0$) within a skin layer. Owing to the disparity of electron and ion mass, an electrostatic field is created in the skin layer by the Lorentz force at the second harmonic of the applied electric field oscillating with frequency ω (see Fig. 29). Since the skin depth is much larger than the Debye length, the skin layer is quasi-neutral, and even small charge separation of the order of 10^{-4} creates noticeable fields in the plasma. The use of low noise Vlasov code is highly beneficial for accurate simulations because the high noise of the particle codes cannot provide required accuracy.

Recently, adaptive grids have been introduced for solving the Vlasov–Poisson system, [100] and efficient data structures for adaptive Vlasov solvers were suggested based on hash table and multilevel arrays [101]. Clearly, research in this direction will continue in the near future.

5.2. Elastic collisions of electrons with atoms

The treatment of electron collisions with heavy species can be simplified using the disparity of mass between colliding partners. The leading term of the collision integral has the form [47]:

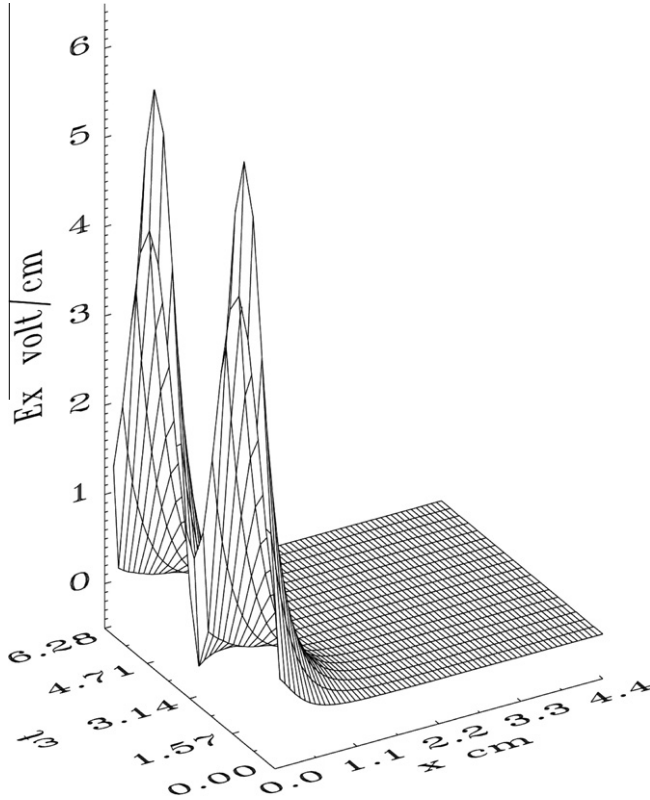


Fig. 29. Spatio-temporal dynamics of longitudinal RF electric field in the skin layer.

$$I_0 = N\xi \int_{S^2} \sigma(\xi, |\Omega - \Omega'|) [f(\xi, \Omega') - f(\xi, \Omega)] d\Omega, \quad (36)$$

where N is the gas density, Ω is a velocity angle on a unit sphere S^2 , and $\xi = \xi\Omega$. The differential collision cross section σ depends on the initial speed and the angle $\theta = \arccos(\Omega \cdot \Omega')$ between electron velocities before and after collision. This term corresponds to an infinitely small mass ratio of colliding particles, when there is no energy exchange between the electron and gas atom. When scattering is close to isotropic, $\sigma(\xi, |\Omega - \Omega'|) = \sigma(\xi)$, the integral (36) is further simplified:

$$I_0 = -v[f(\xi, \Omega) - \int_{S^2} f(\xi, \Omega) d\Omega], \quad (37)$$

where $v = N\xi\sigma(\xi)$ is the collision frequency.

We illustrate dynamically adaptive mesh in velocity space for simulation of the relaxation process described by the collision integral (37) [102]. The velocity space is a unit box: $-0.5 < \xi_x < 0.5$, $-0.5 < \xi_y < 0.5$, $-0.5 < \xi_z < 0.5$. The initial Maxwellian velocity distribution function had a non-zero mean velocity, $V_{0x} = 0.3$, and a temperature $T = 0.005$. Fig. 30 shows the computational mesh and 2D contours of the velocity distribution function at different times. During the relaxation process, a sphere with center at zero and a radius V_{0x} in velocity space is uniformly covered by the particles as a result of large angle scattering. The computational mesh is adapted based on amplitude and gradient of the velocity distribution function. The time evolution of macroparameters is shown in Fig. 31. The density is conserved during the relaxation process. The mean velocity drops to zero in about two collisional times. The temperatures T_x , T_y and T_z evolve towards a single temperature over the same time scale.

6. Electron kinetics in collisional plasmas

Electron kinetics is more complicated and more interesting compared to ion and neutral kinetics because different types of inelastic collisions and ionization events are important for electrons. Peculiarities of electron kinetics in collisional plasmas are due to the disparity of electron and atom mass, $m/M \ll 1$, and a variety of inelastic collision processes (excitation, ionization, chemical reactions) produced by super-thermal electrons. In weakly ionized plasmas, the ratio of plasma to gas density, $\eta = n_e/N$ (ionization degree) is small, and electron collisions with neutral gas species often dominate over Coulomb

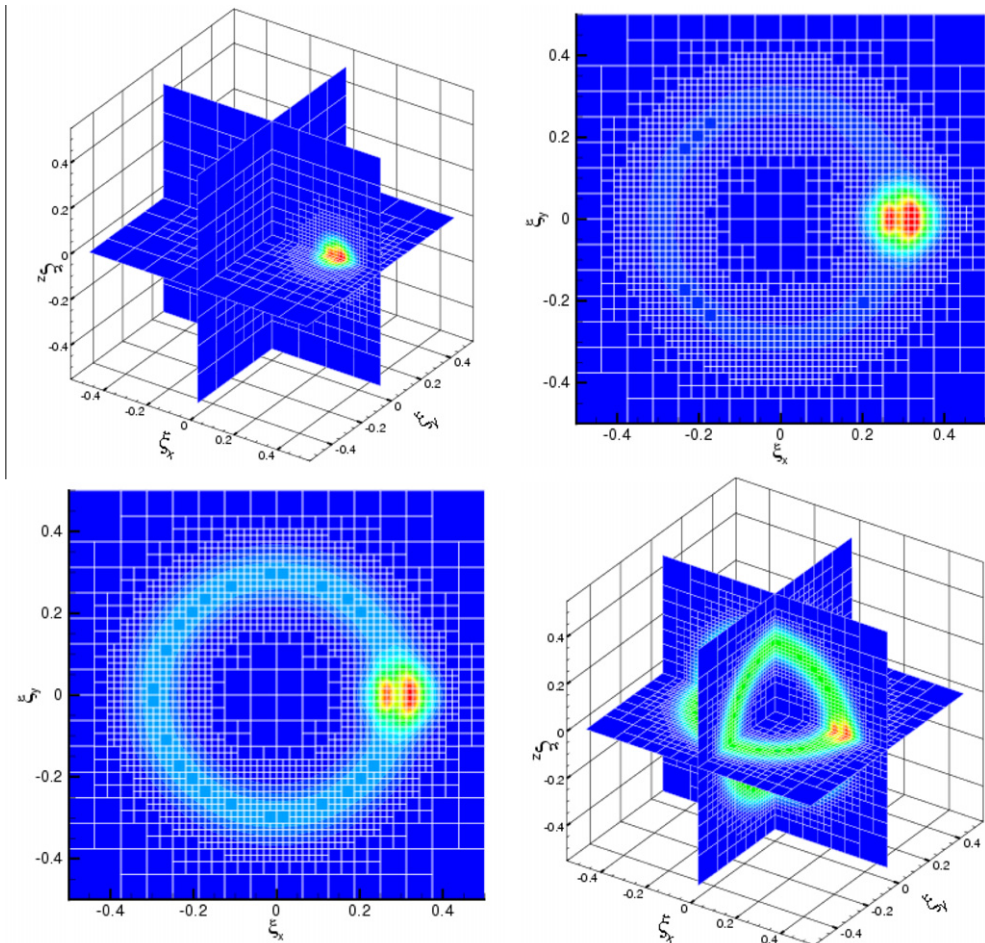


Fig. 30. The computational grid and contours of the velocity distribution functions at dimensionless times $tv = 0.09, 0.45, 1.08, 1.8$ during the relaxation process.

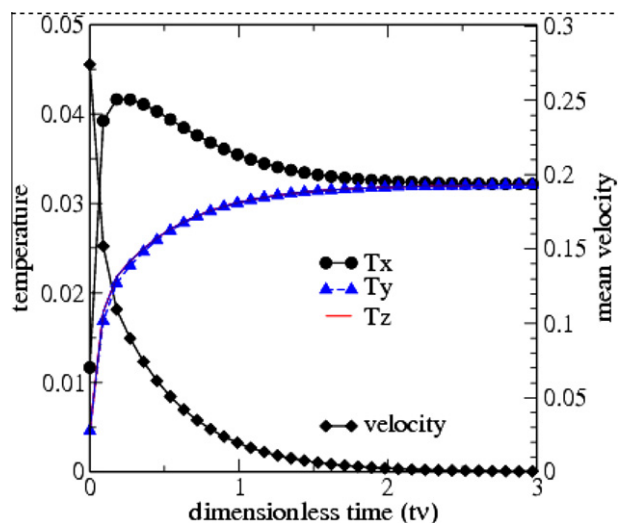


Fig. 31. Time evolution of macro-parameters of a distribution function with initial non-zero velocity.

interactions among charged particles. The first excitation level of atoms, ε_1 , serves a characteristic energy scale for electrons. Depending on electron energy, scattering (changing direction of electron motion) and energy loss in collisions have different importance.

At electron energies of the order of ε_1 (~ 10 eV) the ratio of inelastic to elastic collision frequencies v^*/v is small. As a result of both $m/M \ll 1$ and $v^*/v \ll 1$, kinetic description of these electrons can be reduced to a Fokker–Planck equation using two-term Spherical Harmonics Expansion. Under these conditions, inelastic collisions with large energy loss are relatively rare compared to elastic collisions. The Fokker–Planck approach to electron kinetics has been successfully used for collisional gas discharge plasmas and semiconductor devices [105]. The total energy of electrons (kinetic plus potential) becomes an approximate invariant of the electron motion, and many aspects of gas discharge physics can be interpreted using the concept of total energy for analysis of electron kinetics [103].

For fast electrons, the relative importance of scattering and energy loss is opposite compared to slow electrons. Fast electrons experience small angle scattering and form highly anisotropic velocity distribution functions (electron beams). Strong fields can accelerate electrons to high energies leading to *electron runaway*. In spatially non-uniform fields, the runaway electrons can produce intense non-local ionization in the areas with no electric field. Simultaneous account of scattering and deceleration appears to be rather difficult due to lack of reliable cross-section data for the description of electrons with energies 10–100 eV, especially on angular dependences of inelastic cross-sections.

6.1. Diffusion model for slow electrons

For slow electrons with energy of the order of ε_1 , momentum relaxation in elastic collisions with atoms occurs faster than energy relaxation. The two-term Spherical Harmonics Expansion (SHE) also known as a diffusion approximation or the Lorentz model can be used for these electrons:

$$\frac{\partial f_0}{\partial t} + \frac{\xi}{3} \operatorname{div}(\mathbf{f}_1) + \frac{1}{3\xi^2} \frac{\partial}{\partial \xi} \left(\xi^2 \frac{e\mathbf{E}}{m} \cdot \mathbf{f}_1 \right) = I_1, \quad (38)$$

$$\frac{\partial \mathbf{f}_1}{\partial t} + \xi \nabla f_0 + \frac{e\mathbf{E}}{m} \frac{\partial f_0}{\partial \xi} - \boldsymbol{\omega}_B \times \mathbf{f}_1 = -v_m \mathbf{f}_1. \quad (39)$$

Here, these equations are written in the general 3D form, and include magnetic field

($\boldsymbol{\omega}_B = e\mathbf{B}/m$ is the electron cyclotron frequency vector). The collision integral in the right hand side of (38) describes energy loss in quasi-elastic and inelastic collisions and generation of new electrons in ionization events.

A numerical procedure for solving Eqs. (38) and (39) was developed in [104] for a 2D case using a coupled solver. Retaining the electron inertia term in (39) and using an implicit numerical scheme for the electric field and for the distribution function allowed solving problems where the electric field has complex temporal behavior.

When the time derivative is neglected in (39), one can substitute \mathbf{f}_1 from (39) into (38) to obtain a Fokker–Planck (F–P) kinetic equation for the Electron Energy Distribution Function (EEDF). In the absence of the magnetic field the F–P equation has the form [105]:

$$\frac{\partial f_0}{\partial t} - \nabla \cdot \left[D_r \left(\nabla f_0 + \nabla \varphi \frac{\partial f_0}{\partial u} \right) \right] - \frac{1}{\chi} \frac{\partial}{\partial u} \left[\chi D_r \nabla \varphi \cdot \left(\nabla f_0 + \nabla \varphi \frac{\partial f_0}{\partial u} \right) - \chi \left(V_u f_0 + D_u \frac{\partial f_0}{\partial u} \right) \right] = I_1. \quad (40)$$

Here, electron kinetic energy $u = m_e c^2/(2e)$ (in eV) is used as independent variable, and $\chi(u)$ denotes the density of states ($\chi(u) = \sqrt{u}$ for gaseous plasma). Different terms in Eq. (40) describe: electron diffusion in configuration space with a diffusion coefficient D_r and drift due to electrostatic field, $\mathbf{E} = -\nabla \varphi$; electron heating (cooling) due to the electrostatic field; quasi-elastic processes; inelastic collisions (excitation, ionization, attachment, etc.). The quasi-elastic processes (elastic collisions of electrons with neutrals, excitation of molecular vibrations, Coulomb interactions among electrons and ions) are described in terms of diffusion and convection along the energy axis with coefficients V_u and D_u . Electron heating by RF electric fields can also be included into the energy diffusion coefficient.

6.1.1. The concept of total energy

The Fokker–Planck kinetic Eq. (40) can be simplified [106,107] using total energy $\varepsilon = u - \varphi(\mathbf{r})$ as independent variable instead of kinetic energy u :

$$\frac{\partial f_0}{\partial t} - \frac{\partial \varphi}{\partial t} \frac{\partial f_0}{\partial \varepsilon} - \nabla \cdot D_r \nabla f_0 + \frac{1}{\chi} \frac{\partial}{\partial \varepsilon} \left(\chi \left[D_e(\mathbf{r}, \varepsilon) \frac{\partial f_0}{\partial \varepsilon} + V_e(\mathbf{r}, \varepsilon) f_0 \right] \right) = I. \quad (41)$$

This equation describes diffusion of electrons over accessible area of the discharge bounded by the surface $\varepsilon = -\varphi(\mathbf{r})$ on which electron kinetic energy is zero. The accessible area could be quite different for electrons with different total energy. Under low-pressure conditions, spatial diffusion of electrons occurs fast (the third term in (41) dominates over the fourth term), and electrons with different total energy diffuse quite independently. Kinetic energy of the electrons depends on the local value of the electric potential, and has maximal value where the potential energy $\varphi(\mathbf{r})$ is minimal. In this area inelastic processes described by the right hand side of (41) take place.

The concept of total electron energy has demonstrated its value for understanding many problems of gas discharge physics. It was rediscovered independently for modeling electron kinetics in semiconductor devices [108,109], and implemented in the commercial software CFD-ACE [105]. Many interesting results were obtained [110] for the conditions when the characteristic spatial scale L is larger than electron mean free path λ but comparable to electron energy relaxation length λ_e . The latter can exceed λ by orders of magnitude due to the disparity of the electron to atom mass. In this *non-local* regime, the EEDF, f_0 , at a given point depends not only on the electric fields at this point but also by plasma properties in the vicinity of the point of the size λ_e (a memory effect). In this collision-dominated regime, a number of interesting non-local kinetic effects take place [111]. The most interesting example is ionization waves (striations) demonstrating complicated self-organization at kinetic level [112].

6.2. Fast runaway electrons

At high values of E/N , electrons can be continuously accelerated by electric fields forming highly anisotropic velocity distributions aligned along the direction of the field. The energy loss of fast electrons can be described in the continuous slowing down approximation:

$$m \frac{\partial \xi}{\partial t} = eE\mu - NL(u), \quad (42)$$

$$\frac{\partial \mu}{\partial t} = \frac{eE(1 - \mu^2)}{m\xi}, \quad (43)$$

where μ is the cosines of polar angle between electron velocity and the direction of the electric field, and $L(u)$ is an energy loss function. Fig. 32 shows examples of the energy loss function, which has a maximum at energies of the order of 100 eV, and coincides with the Bethe–Bloch law at high electron energies.

The condition

$$eE\mu > NL_{\max} \quad (44)$$

corresponds to electron runaway, when electrons are continuously accelerated by the electric field. The flux of runaway electrons is determined by peculiarities of scattering at electron energies ~ 100 eV near the maximum of $L(u)$.

For simple analysis of electron runaway in non-uniform electric fields, one can completely neglect the electron scattering and use the kinetic equation in the form [113]:

$$\frac{\partial f}{\partial t} + \xi \frac{\partial f}{\partial x} - \frac{eE(x, t)}{m} \frac{\partial f}{\partial \xi} - \frac{\partial}{\partial \xi} \frac{NL(u)}{m} = I(x, \xi, t). \quad (45)$$

Here, the source term $I(x, \xi, t)$ describes the generation of new electrons in ionization events. The simplest form of the ionization term

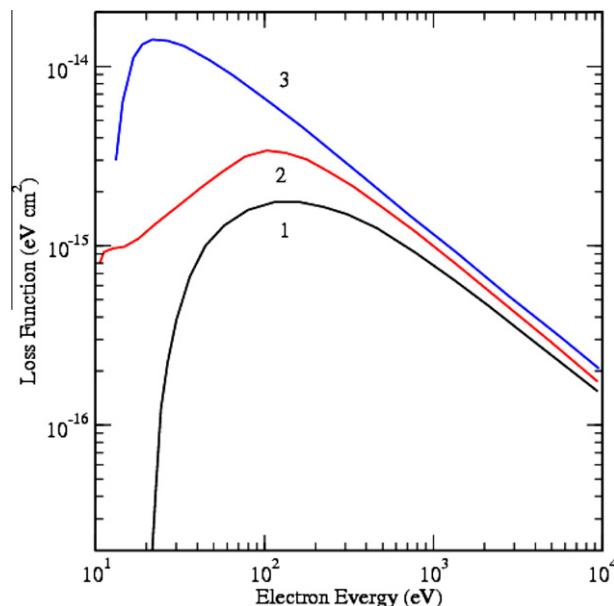


Fig. 32. The energy loss function for Hydrogen (1) and Helium (2). Curve (3) is the Bethe–Bloch law for Helium [113].

$$I(\xi) = \delta(\xi) \int_0^\infty \frac{L(u)}{\varepsilon_0} \xi' f(\xi') d\xi' \quad (46)$$

assumes that the secondary electrons are born with zero kinetic energy, and the energy cost per ionization event is ε_0 .

Assuming $L(u) \approx L_0 = \text{const}$, one can introduce total energy, $\varepsilon = u - NL_0x - \varphi(x)$ and obtain an analytical solution of (45) in the form [113]

$$f(\varepsilon) = \delta(\varepsilon - 1) - \frac{\alpha \bar{\phi}_c}{\tilde{E}(x_0(\tilde{\varepsilon}))} \exp(\alpha x_0(\tilde{\varepsilon})), \quad (47)$$

where $\alpha = NL_0/\varepsilon_0$ is the maximal value of the first Townsend coefficient. Fig. 33 illustrates the physical meaning of this solution for a typical case of the cathode region in DC glow discharges. The electric field is assumed to be linear in the sheath, $E(x) = E_0(1 - x/d)$, and zero in the plasma (at $x > d$). The electrostatic potential is parabolic, $\varphi(x) = \varphi_c(1 - x/d)^2$. The effective potential, $\phi(x) = \varphi(x) - NL_0/e$, is also parabolic, $\phi(x) = \phi_c(1 - x/\tilde{d})^2$, where \tilde{d} is the point inside the sheath where the total force, $\tilde{E} = -\partial\phi/\partial x$, is equal to zero (see Fig. 33). The first term in (47) describes the primary electrons ejected from the cathode. These electrons penetrate the distance $\Lambda = \frac{e\varphi_c}{NL_0}$ before losing their energy. The second term describes electrons generated in the cathode sheath, at $x < \tilde{d}$. These electrons are capable of further multiplication. For example, the secondary electrons generated at x_0 lose all their energy at $x = x_1$.

More sophisticated models with simultaneous account for small angle scattering and deceleration have been developed to study electron kinetics in atmospheric breakdown [114,115]. With account for small angle scattering, the kinetic equation has the form [116]

$$\frac{\partial f}{\partial t} + \frac{p}{m} \frac{\partial f}{\partial x} + \frac{1}{p^2} \frac{\partial}{\partial p} \{p^2(NL - eE\mu)f\} - \frac{\partial}{\partial \mu} \left\{ (1 - \mu^2) \left(\frac{eE}{p} f + D \frac{\partial f}{\partial \mu} \right) \right\} = I, \quad (48)$$

where, $p = m\xi$ is electron momentum. Near the boundary of the runaway region, where p changes relatively slowly, one can expect that the angular distribution is formed faster than the changes in p . The equation for the angular distribution can be obtained by equating the $\partial/\partial\mu$ term to zero [117]:

$$F = C(p, t) \exp \left(\mu \frac{eE}{pD} \right). \quad (49)$$

By substituting the self-similar distribution (49) into (48) and averaging over angles, one obtains for a spatially homogeneous case:

$$\frac{\partial f}{\partial t} - \frac{1}{p^2} \frac{\partial}{\partial p} \{p^2(NL - eEM(p))F\} = \Upsilon, \quad (50)$$

where the function $M(p) = \frac{1}{2F} \int_{-1}^1 \mu f d\mu$ is the average value of μ for a given p , and $\Upsilon = \frac{1}{2F} \int_{-1}^1 I_2 d\mu$ is the averaged value of the electron production term. The total number of runaway electrons can be found from (50). It is interesting that small angle

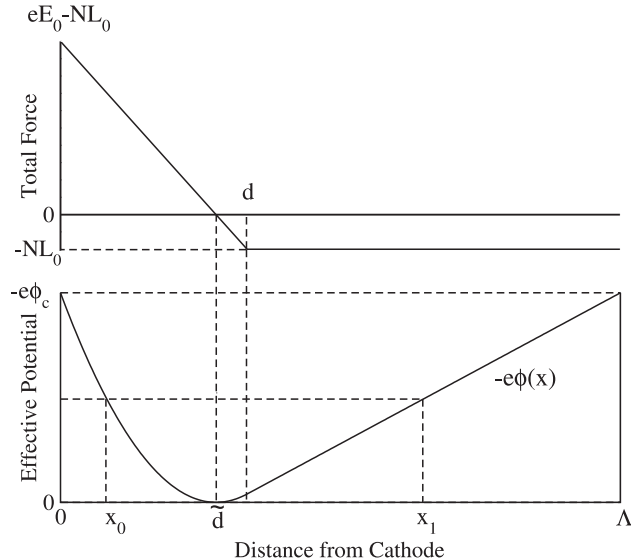


Fig. 33. (a) Total force acting on electrons, and (b) effective potential energy.

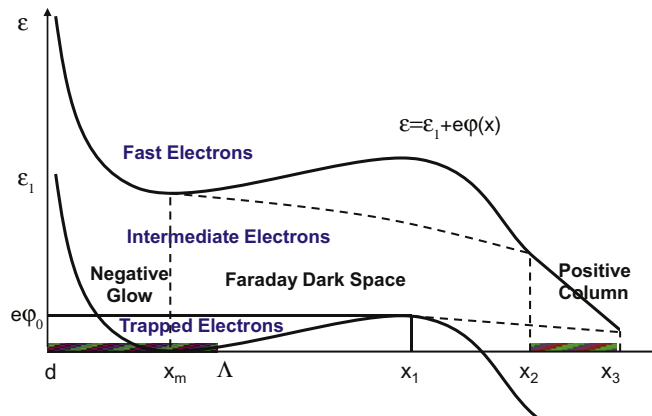


Fig. 34. Potential profile in the cathode region, and formation of three groups of electrons.

scattering could substantially modify the particle trajectories in phase space and the electron diffusion in μ space can affect the runaway criterion (44) and the flux of runaway electrons [118].

Numerical solution of Eq. (48) can be obtained by traditional methods of computational fluid dynamics. For a spatially homogeneous case, the finite volume solution of the relativistic Boltzmann equation for electron avalanche studies was demonstrated in [114]. Adaptive mesh refinement in velocity space appears to be attractive for accurate resolution of highly anisotropic velocity distributions with long tails corresponding to runaway electrons.

6.3. Electron groups in the cathode region of DC glow discharges

The cathode region of DC glow discharges is a perfect example of a problem where three distinct groups of electrons can be easily identified [113]. The first group includes primary electrons injected from the cathode by ion impact and accelerated in the cathode sheath. This group also includes the secondary electrons which are produced in the sheath by electron impact and initiate electron avalanches. The condition of electron runaway (44) is usually satisfied inside the sheath, and this group of electrons is characterized by strong anisotropy and described by the models (45) and (48). These electrons are responsible for non-local ionization in the negative glow and electric field reversal in the cathode region (see Fig. 34).

The second group of electrons includes those produced in the negative glow region outside the sheath. These electrons are responsible for the current transfer in the Faraday Dark Space (FDS) between points x_1 and x_2 in Fig. 34. They can be well described by the Fokker Planck Eq. (41) for the EEDF. These electrons are responsible for the ionization in the region $x > x_2$, and the transition from the FDS to positive column.

The third group of electrons includes those trapped by the electrostatic potential in the cathode region. The characteristic energy of these electrons is of the order of potential well, $e\varphi_0$. These electrons do not participate in the current flow and are responsible for a sharp peak of plasma density at the point x_m where the electric potential has a local minimum. The EEDF of these electrons is often Maxwellian, their density is defined by the Boltzmann relation and the temperature is slightly above the room temperature [113].

7. Conclusions

We have described an Adaptive Mesh and Algorithm Refinement (AMAR) methodology for multi-scale simulations of gas flows and the challenges associated with extending this methodology for simulations of weakly ionized plasmas. The basic principle of the AMAR methodology is to use kinetic methods only in those areas of phase space where they are required. Our implementation of the AMAR is based on octree Cartesian mesh and discrete velocity models for solving kinetic equations. Using similar numerical techniques for solving kinetic and fluid equations allows for seamless coupling of atomistic and continuum models. We have described a Unified Flow Solver with AMAR methodology for simulations of gas dynamics including recent extensions for multi-component reactive flows of molecular gases and gas mixtures. The challenges of extending the AMAR technology to weakly ionized plasmas have been identified; they are mainly associated with distinct scales between electron and heavy particle transport. We have demonstrated fluid plasma simulations with AMR capabilities using physical models of different complexity. We have described deterministic kinetic solvers for electrons, which can be used under different conditions. The incorporation of electron kinetics into AMAR methodology is a subject of current research.

The development of adaptive multi-scale models of weakly ionized plasmas is important for understanding streamers and spark discharges, luminous layers in the upper atmosphere, filaments in dielectric barrier discharges, and nanosecond breakdown of dense gases driven by runaway electrons. The development of these capabilities will help uncover the mysteries of lightning, and advance current and future technologies utilizing cold plasmas.

Acknowledgements

This work was partially supported by the US Air Force STTR Project FA9550-10-C-0053 and NASA SBIR Project NNX10CB32C. We wish to thank Drs V. Aristov, A. Frolova and S. Zabelok for their contributions to UFS development and useful discussions. Thanks to Magdi Shoucri for sharing with us his Vlasov codes.

References

- [1] C. Cercignani, The Boltzmann Equation and its Applications, Springer-Verlag, 1988.
- [2] Y. Sone, Kinetic Theory and Fluid Dynamics, Burkhausen, Boston, 2002.
- [3] C.K. Birdsall, A.B. Langdon, Plasma Physics via Computer Simulations, Taylor and Francis, 2004.
- [4] J.P. Verboncoeur, Particle simulation of plasmas: review and advances, *Plasma Phys. Control. Fusion* 47 (2005) A231.
- [5] G.A. Bird, Molecular Gas Dynamics and the Direct Simulation of Gas Flows, Oxford Science Publications, 1994.
- [6] I.D. Boyd, Direct simulation monte carlo for atmospheric entry, in: Non-equilibrium Gas Dynamics from Physical Models to Hypersonic Flights, RTO-EN-AVT-162, 2009.
- [7] V.V. Aristov, Direct Methods for Solving the Boltzmann Equation and Study of Non-Equilibrium Flows, Kluwer Academic Publishers, Dordrecht, 2001.
- [8] F.G. Tcherevmissine, Direct numerical solution of the Boltzmann equation, *AIP Conf. Proc.* 762 (2005) 677–685;
- F.G. Tcherevmissine, Solution of the Boltzmann equation for high-speed flows, *Comput. Math. Math. Phys.* 46 (2006) 315;
- F.G. Tcherevmissine, Solution of the Boltzmann equation for low-speed flows, *Transport Theory Stat. Phys.* 37 (2008) 564.
- [9] M. Shoucri (Ed.), Eulerian Codes for the Numerical Solution of the Kinetic Equations of Plasmas, Nova Publishers, 2010.
- [10] P. Degond, L. Pareschi, G. Russo (Eds.), Modeling and Computational methods for Kinetic Equations, Birkhauser, Boston, 2004, p. 356.
- [11] C. Mouhot, L. Pareschi, Fast algorithms for computing the Boltzmann collision operator, *Math. Comput.* 75 (2006) 1833.
- [12] P. Kowalczyk et al, Numerical solutions of the Boltzmann equation: comparison of different algorithms, *Eur. J. Mech. B* 27 (2008) 62.
- [13] I. Ibragimov, S. Rjasanov, Three way decomposition for the Boltzmann equation, *J. Comput. Math.* 27 (2009) 184.
- [14] U. Kortshagen, L.D. Tsendin (Eds.), Electron Kinetics and Applications of Glow Discharges, NATO ASI Series, vol. 367, Kluwer Academic Publishers, 1998.
- [15] M.J. Kushner, Hybrid modelling of low temperature plasmas for fundamental investigation and equipment design, *J. Phys. D* 42 (2009) 194013.
- [16] H.S. Wijesinghe, N.G. Hadjiconstantinou, A discussion of hybrid atomistic-continuum methods for multiscale hydrodynamics, *Int. J. Multiscale Comput. Eng.* 2 (2004) 189.
- [17] V.I. Kolobov, S.A. Bayyuk, R.R. Arslanbekov, V.V. Aristov, A.A. Frolova, S.A. Zabelok, Construction of a unified continuum/kinetic solver for aerodynamic problems, *AIAA J. Spacecraft Rockets* 42 (2005) 598–605.
- [18] J.F. Bourgat, P. Le Tallec, M.D. Tidriri, Coupling Boltzmann and Navier–Stokes equations by friction, *J. Comput. Phys.* 127 (1996) 227.
- [19] S. Tiwari, A. Klar, An adaptive domain decomposition procedure for Boltzmann and Euler equations, *J. Comput. Appl. Math.* 90 (1998) 223.
- [20] P. Le Tallec, F. Mallinger, Coupling Boltzmann and Navier–Stokes equations by half fluxes, *J. Comput. Phys.* 136 (1997) 51.
- [21] S. Tiwari, Coupling of the Boltzmann and Euler equations with automatic domain decomposition, *J. Comput. Phys.* 144 (1998) 710.
- [22] T. Ohsawa, T. Ohwada, Deterministic hybrid computation of rarefied gas flows, in: Rarefied Gas Dynamics: 23rd International Symposium, Andrew D. Ketsdever, E.P. Munz, (Eds.), AIP Conference Proceedings vol. 663, 2003, pp. 931–938.
- [23] T.E. Schwartzenuber, L.C. Scalabrin, I.D. Boyd, A modular particle-continuum numerical method for hypersonic non-equilibrium gas flows, *J. Comput. Phys.* 225 (2007) 1159.
- [24] P. Degond, G. Dimarco, L. Mieussens, A multiscale kinetic-fluid solver with dynamic localization of kinetic effects, *J. Comput. Phys.* 229 (2010) 4907.
- [25] A.E. Beylich, Solving the kinetic equation for all Knudsen numbers, *Phys. Fluids* 12 (2000) 444.
- [26] N. Crouseilles, P. Degond, M. Lemou, A hybrid kinetic/fluid models for solving the gas dynamics Boltzmann–BGK equation, *J. Comput. Phys.* 199 (2004) 776.
- [27] H.C. Kim, F. Iza, S.S. Yang, M. Radmilovic-Radjenovic, J.K. Lee, Particle and fluid simulations of low temperature plasma discharges: benchmark and kinetic effects, *J. Phys. D* 38 (2005) R283.
- [28] L. Tsendin, Nonlocal electron kinetics in gas-discharge plasma, *Physics –Uspekhi* 53 (2010) 133.
- [29] D.B. Hash, H.A. Hassan, Two-dimensional coupling issues of hybrid DSMC/Navier–Stokes solvers, in: AIAA Paper 97-2507, 1997.
- [30] H.A. Carlson, R. Roveda, I.D. Boyd, G.V. Candler, A hybrid CFD-DSMC method of modeling continuum-rarefied flows, in: AIAA Paper 2004-1180, 2004.
- [31] L.L. Baker, N.G. Hadjiconstantinou, Variance reduction for Monte Carlo solution of the Boltzmann equation, *Phys. Fluids* 17 (2005) 051703.
- [32] S. Tiwari, A. Klar, S. Hardt, A particle-particle hybrid method for kinetic and continuum equations, *J. Comput. Phys.* 228 (2010) 7109.
- [33] A.L. Garsia, J.B. Bell, W.Y. Crutchfield, B.J. Alder, Adaptive mesh and algorithm refinement using direct simulation monte carlo, *J. Comput. Phys.* 54 (1999) 134.
- [34] S.P. Popov, F.G. Tcherevmissine, A conservative method for solving the Boltzmann equation with centrally symmetric interaction potentials, *Comput. Math. Math. Phys.* 39 (1999) 156.
- [35] S. Succi, The Lattice Boltzmann Equation for Fluid Dynamics and Beyond, Oxford University Press, 2001.
- [36] N.M. Korobov, Exponential Sums and Their Applications, Springer, 2001, p. 232; Theoretico-Numerical Methods in Approximate Analysis, Moscow 2004 (in Russian).
- [37] A.B. Morris, P.L. Varghese, D.B. Goldstein, Monte Carlo solution of the Boltzmann equation via a discrete velocity model, *J. Comput. Phys.* 230 (2011) 1265.
- [38] Yu.Yu. Kloss, P.V. Shuvalov, F.G. Tcherevmissine, Solving Boltzmann equation on GPU, *Proc. Comput. Sci.* 1 (2010) 1077.
- [39] A. Frezzotti, et al, Solving Kinetic Equations on GPUs, arXiv:0903.4044v1 [physics.comp-ph] 24 March, 2009.
- [40] A.E. Beylich, Kinetics of thermalization in shock waves, *Phys. Fluids* 14 (2002) 2683.
- [41] T. Ohwada, Structure of normal shock waves on the basis of the Boltzmann equation for hard-spheres molecules, *Phys. Fluids* A5 (1993) 217–234.
- [42] V.V. Aristov, Method of adaptive meshes in velocity space for the intense shock wave problems, *J. Comput. Math. Math. Phys.* 17 (1977) 261.
- [43] A. Heintz et al, Fast numerical method for the Boltzmann equation on non-uniform grids, *J. Comput. Phys.* 227 (2008) 6681.
- [44] S. Kozuge, K. Aoki, S. Takata, Shock wave structure of a binary gas mixture: finite-difference analysis of the Boltzmann equation for hard-sphere molecules, *Eur. J. Mech. B – Fluids* 20 (2001) 87.
- [45] A. Raines, Study of shock wave structure in gas mixtures on the basis of the Boltzmann equation, *Eur. J. Phys. B* 21 (2002) 599.
- [46] E. Josyula, P. Vedula, W.F. Bailey, C.J. Suchyta, Kinetic solution of the structure of a shock wave in a nonreactive gas mixture, *Phys. Fluids* 23 (2011) 017101.
- [47] P.P.J.M. Schram, Kinetic Theory of Gases and Plasmas, Springer, 1991.
- [48] F.G. Tcherevmissine, Solution of the Wang–Chang–Uhlenbeck master equation, *Doklady Phys.* 47 (2002) 872.
- [49] F.G. Tcherevmissine, V.I. Kolobov, R.R. Arslanbekov, Simulation of shock wave structure in nitrogen with realistic rotational spectrum and molecular interaction potential, in: Proceedings of 25th Rarefied Gas Dynamics Symposium M.S. Ivanov, A.K. Rebrov, Novosibirsk (Eds.), 2007.
- [50] K. Koura, Direct simulation Monte Carlo study of rotational nonequilibrium in shock wave and spherical expansion of nitrogen using classical trajectory calculations, *Phys. Fluids* 14 (2002) 1689.
- [51] V.A. Rykov, V.A. Titarev, E.M. Shakhor, *J. Comput. Math. Math. Phys.* 47 (2007) 144.

- [52] M. Groppi, K. Aoki, G. Spiga, V. Tritsch, Shock structure analysis in chemically reacting gas mixtures by a relaxation time kinetic model, *Phys. Fluids* 20 (2008) 117103.
- [53] A.M. Starik, N.S. Titova, I.V. Arsentiev, Comprehensive analysis of the effect of atomic and molecular metastable state excitation on air plasma composition behind strong shock waves, *Plasma Sources Sci. Technol.* 19 (2010) 015007.
- [54] M.N. Shneider, P.F. Barker, S.F. Gimelshein, Molecular transport in pulsed optical lattices, *Appl. Phys. A* (2007), doi:[10.1007/s00339-007-4113-7](https://doi.org/10.1007/s00339-007-4113-7).
- [55] V. Kolobov, et al, Unified Kinetic Approach for Simulations of Gas Flows in Rarefied and Continuum Regimes, Report AFRL-RB-WP-TR-2008-3031, 2008.
- [56] V.I. Kolobov, R.R. Arslanbekov, V.V. Aristov, A.A. Frolova, S.A. Zabelok, Unified solver for rarefied and continuum flows with adaptive mesh and algorithm refinement, *J. Comput. Phys.* 223 (2007) 589.
- [57] H. Samet, The quadtree and related hierarchical data structures, *Comput. Surv.* 16 (1984) 187; H. Samet, Foundations of Multidimensional and Metric Data Structures, Elsevier, 2006.
- [58] C. Burstedde, L.C. Wilcox, O. Ghattas, p4est: Scalable Algorithms for Parallel Adaptive Mesh Refinement on Forests of Octrees, *SIAM Journal of Scientific Computing* 33 (2011) 1103–1133.
- [59] M.L. Norman, The impact of AMR in numerical astrophysics and cosmology, in: Adaptive Mesh Refinement – Theory and Applications, Lecture Notes in Computational Science and Engineering, Springer, 2005.
- [60] S. Popinet, Gerris: a tree-based adaptive solver for the incompressible Euler equations in complex geometries, *J. Comput. Phys.* 190 (2003) 572.
- [61] H. Sagan, Space Filling Curves, Springer, 1994.
- [62] L. Stocco, G. Schrack, On spatial orders and location codes, *IEEE Trans. Comput.* 58 (2009) 424.
- [63] G. Agbaglah, et al, Parallel simulation of multiphase flows using octree adaptivity and the volume-of-fluid model, *C.R. Mech.* (2011), doi:[10.1016/j.crme.2010.12.006](https://doi.org/10.1016/j.crme.2010.12.006).
- [64] A.M. Khokhlov, Fully threaded tree algorithms for adaptive refinement fluid dynamics simulations, *J. Comput. Phys.* 143 (1998) 519.
- [65] S. Muller, Adaptive multiscale schemes for conservation laws, Lecture Notes on Computational Science and Engineering, vol. 27, Springer, 2002.
- [66] H. Ji, F.-S. Lien, E. Yee, A new adaptive mesh refinement data structure with an application to detonation, *J. Comput. Phys.* 229 (2010) 8981.
- [67] D. Madeira, T. Leviner, GPU Octree and Optimized Search, VIII Brazilian Symposium on Games and Digital Entertainment, Rio de Janeiro , 2009.
- [68] T. Ohwada, On the construction of kinetic schemes, *J. Comput. Phys.* 177 (2002) 156.
- [69] K. Xu, J.-C. Chen, A unified gas kinetic scheme for continuum and rarefied flows, *J. Comput. Phys.* 229 (2010) 7747.
- [70] C.K. Aodun, J.R. Clausen, Lattice Boltzmann method for complex flows, *Ann. Rev. Fluid Mech.* 42 (2010) 439.
- [71] W.J. Courier, An Adaptively Refined, Cartesian Cell-Based Scheme for the Euler and Navier–Stokes Equations, Ph.D. Thesis, University of Michigan, Ann Arbor, 1993.
- [72] J.D. Lee, S.M. Ruffin, Development of a turbulent wall-function based viscous Cartesian-grid methodology, in: AIAA-2007-1326, 2007.
- [73] C.S. Peskin, The immersed boundary method, *Acta Numer.* (2002) 1.
- [74] R. Mittal, G. Iaccarino, Immersed boundary methods, *Ann. Rev. Fluid Mech.* 37 (2005) 239.
- [75] R. Dillon, Zhilin Li, An introduction to the immersed boundary and the immersed interface methods, in: Interface Problems and Methods in Biological and Physical Flows, World Scientific Publishing Co, 2009.
- [76] M.D. de Tullio et al, An immersed boundary method for compressible flows using local grid refinement, *J. Comput. Phys.* 225 (2007) 2098.
- [77] R. Ghias, R. Mittal, H. Dong, "A sharp interface immersed boundary method for compressible viscous flows, *J. Comput. Phys.* 225 (2007) 528.
- [78] R.R. Arslanbekov, V.I. Kolobov, A.A. Frolova, Immersed boundary method for Boltzmann and Navier–Stokes solvers with adaptive cartesian mesh, in: 27th International Symposium On Rarefied Gas Dynamics, AIP Conf. Proc. vol. 1333, 2011, pp. 873–877, doi:[10.1063/1.3562755](https://doi.org/10.1063/1.3562755).
- [79] S. Dellacherie, Coupling of the Wang Chang–Uhlenbeck equations with the multispecies Euler system, *J. Comput. Phys.* 189 (2003) 239.
- [80] V.I. Kolobov, K. Ikeda, T. Okumura, 3D simulations of an industrial ICP reactor with comparison to experimental data, in: 30th IEEE International Conference on Plasma Science, Plasma Science, 2003. ICOPS 2003. IEEE Conference Record – Abstracts The 30th International Conference on Plasma Science, 2003, p. 460.
- [81] G.E. Georgiou, A.P. Papadakis, R. Morrow, A C Metaxas, Numerical modeling of atmospheric pressure gas discharges leading to plasma production, *J. Phys. D* 38 (2005) R303.
- [82] C.-C. Wang, S. Roy, Three-dimensional simulation of a microplasma pump, *J. Phys. D* 42 (2009) 185206.
- [83] P. Colella, M.R. Dorr, D.D. Wake, Numerical solution of plasma fluid equations using locally refined grids, *J. Comput. Phys.* 152 (1999) 550.
- [84] T. Unfer, J.-P. Boeuf, et al, Multi-scale gas discharge simulations using asynchronous adaptive mesh refinement, *Comput. Phys. Commun.* 181 (2010) 247.
- [85] W-G. Min et al, A study of the streamer simulation using adaptive mesh generation and FEM-FCT, *IEEE Trans. Magn.* 37 (2001) 3141.
- [86] C. Montijn et al, An adaptive grid refinement strategy for the simulation of negative streamers, *J. Comput. Phys.* 219 (2006) 801.
- [87] D.S. Nikandrov, R.R. Arslanbekov, V.I. Kolobov, Streamer simulations with dynamically adaptive Cartesian mesh, *IEEE TPS* 36 (2008) 932.
- [88] S. Pancheshnyi, P. Segur, J. Capeillere, A. Bourdon, Numerical simulation of filamentary discharges with parallel adaptive mesh refinement, *J. Comput. Phys.* 227 (2008) 6574.
- [89] M.I. Dyakonov, V.Y. Kachorovskii, Streamer discharge in a homogeneous field, *Sov. Phys. JETP* 68 (1989) 1070.
- [90] Yu Akishev et al, Negative corona, glow and spark discharges in ambient air and transitions between them, *Plasma Sources Sci. Technol.* 14 (2005) S18.
- [91] P. Tardieuau, N. Moreau, S. Bentaleb, et al, Diffuse mode and diffuse-to-filamentary transition in a high pressure nanosecond scale corona discharge under high voltage, *J. Phys. D* 42 (2009) 175202.
- [92] T.N. Tran, I.O. Golosnoy, P.L. Levin, G.E. Georgiou, Numerical modeling of negative corona discharges in air with experimental validation, *J. Phys. D* 44 (2010) 015203.
- [93] O. Charion, T. Neubert, Production of runaway electrons by negative streamer discharges, *J. Geophys. Res.* 115 (2010) A00E32, doi:[10.1029/2009JA014774](https://doi.org/10.1029/2009JA014774).
- [94] N.Yu. Babaeva, M.J. Kushner, Effect of inhomogeneities on streamer propagation, *Plasma Sources Sci. Technol.* 18 (2009) 035009.
- [95] C. Li, U. Ebert, W. Hundsdorfer, Spatially hybrid simulations for streamer discharges with generic features of pulled fronts, *J. Comput. Phys.* 229 (2010) 200.
- [96] M. Shoucri, Numerical Solution of Hyperbolic Differential Equations, Nova Science Publishers, 2008.
- [97] V.I. Kolobov, R.R. Arslanbekov, A.A. Frolova, Multi-scale simulations of gas flows: effect of external forces, rarified gas dynamics, in: Proceedings of the 26th International Symposium on Rarefied Gas Dynamics, AIP Conference Proceedings, vol. 1084, 2008, pp. 441–446.
- [98] V.A. Godoyk, Hot plasma effects in gas discharge plasma, *Phys. Plasmas* 12 (2005) 055501.
- [99] M. Shoucri, J.P. Matte, A. Cote, Numerical simulation of an inductively coupled discharge using an Eulerian Vlasov code, *J. Phys. D* 36 (2003) 2083.
- [100] E. Sonnendrücker, Adaptive methods for the Vlasov equation, in: MAMCDP09 workshop, 2009.
- [101] O. Hoenen, E. Violard, An Efficient Data Structure for an Adaptive Vlasov Solver, research report, <http://icps.u-strasbg.fr/pub_list.php?authors=hoenen&pres=0>.
- [102] V.I. Kolobov, R.R. Arslanbekov, A.A. Frolova, Boltzmann solver with adaptive mesh in velocity space, in: 27th International Symposium on Rarefied Gas Dynamics, AIP Conf. Proc. vol. 1333, 2011, pp. 928–933, doi:[10.1063/1.3562764](https://doi.org/10.1063/1.3562764).
- [103] A.A. Kudryavtsev, A.S. Smirnov, L.D. Tsednik, Physics of Glow Discharges (2010) (in Russian).
- [104] R.J. Kingham, A.R. Bell, An implicit Vlasov–Fokker–Planck code to model non-local electron transport in 2-D with magnetic fields, *J. Comput. Phys.* 194 (2004) 1.
- [105] V.I. Kolobov, Fokker Planck modeling of electron kinetics in plasmas and semiconductors, *Comput. Mater. Sci.* 28 (2003) 302.

- [106] L.D. Tsendin, Electron distribution function of weakly ionized plasmas in nonuniform electric fields, Sov. J. Plasma Phys. 8 (1982) 96.
- [107] J.R. Albritton, Laser absorption and heat transport by non-Maxwell–Boltzmann electron distribution, Phys. Rev. Lett. 50 (1983) 2078.
- [108] W. Liang, N. Goldsman, I. Meyergoyz, 2-D MOSFET modeling including surface effects and impact ionization by self-consistent solution of the boltzmann, poisson, and hole-continuity equations, IEEE Trans. Electron Devices 44 (1997) 257.
- [109] K. Rahmat, J. White, D.A. Antoniadis, Simulation of semiconductor devices using a Galerkin/SHE approach to solving the coupled Poisson–Boltzmann system, IEEE Trans. Comput. Aided Des. Integr. Circuits Syst. 15 (1996) 1181.
- [110] V.I. Kolobov, R.R. Arslanbekov, Simulation of electron kinetics in gas discharges, IEEE Trans. Plasma Sci. 34 (2006) 895.
- [111] V.I. Kolobov, V.A. Godyak, Non-local electron kinetics in collisional gas discharge plasmas, IEEE Trans. Plasma Sci. 23 (1995) 503.
- [112] V.I. Kolobov, Striations in rare gas plasmas (Topical Review), J. Phys. D. 39 (2006) R487–R506.
- [113] V.I. Kolobov, L.D. Tsendin, Analytic model of short gas discharge in light gases, Phys. Rev. A 46 (1992) 7837.
- [114] E.M.D. Symbalisty, R-A. Russel-Dupre, V.A. Yukhimuk, Finite volume solution of the relativistic Boltzmann equation for electron avalanche studies, IEEE Trans. Plasma Sci. 26 (1998) 1575.
- [115] A.A. Solovyev et al, Electron kinetic effects in atmospheric breakdown by an intense electromagnetic pulse, Phys. Rev. E 60 (1999) 7360.
- [116] D.S. Nikandrov, Formation of distribution function of runaway electrons in strong field of pulsed gas discharges, Tech. Phys. 53 (2008) 1565.
- [117] N.G. Lehtinen, T.F. Bell, U.S. Inan, Monte Carlo simulation of runaway MeV electron breakdown with application to red sprites and terrestrial gamma ray flashes, J. Geophys. Res. 104 (1999) 24,69.
- [118] M. Bakhtiari, Revisiting the momentum-space study of runaway electrons during lightning initiation, J. Phys. D. 42 (2009) 015209.